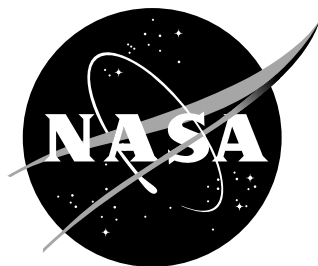NASA/TM–2008–215342

# An Initial Investigation of the Effects of Turbulence Models on the Convergence of the RK/Implicit Scheme

*R. C. Swanson*
*Langley Research Center, Hampton, Virginia*

*C.-C. Rossow*
*DLR, Deutsches Zentrum für Luft- und Raumfahrt,*
*Institut für Aerodynamik und Strömungstechnik,*
*Braunschweig, Germany*

August 2008

Since its founding, NASA has been dedicated to the advancement of aeronautics and space science. The NASA Scientific and Technical Information (STI) Program Office plays a key part in helping NASA maintain this important role.

The NASA STI Program Office is operated by Langley Research Center, the lead center for NASA's scientific and technical information. The NASA STI Program Office provides access to the NASA STI Database, the largest collection of aeronautical and space science STI in the world. The Program Office is also NASA's institutional mechanism for disseminating the results of its research and development activities. These results are published by NASA in the NASA STI Report Series, which includes the following report types:

- TECHNICAL PUBLICATION. Reports of completed research or a major significant phase of research that present the results of NASA programs and include extensive data or theoretical analysis. Includes compilations of significant scientific and technical data and information deemed to be of continuing reference value. NASA counterpart of peer-reviewed formal professional papers, but having less stringent limitations on manuscript length and extent of graphic presentations.

- TECHNICAL MEMORANDUM. Scientific and technical findings that are preliminary or of specialized interest, e.g., quick release reports, working papers, and bibliographies that contain minimal annotation. Does not contain extensive analysis.

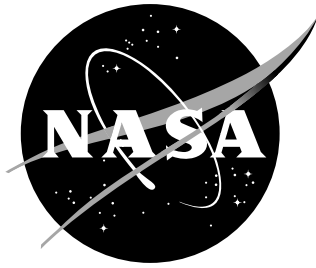- CONTRACTOR REPORT. Scientific and technical findings by NASA-sponsored contractors and grantees.

- CONFERENCE PUBLICATION. Collected papers from scientific and technical conferences, symposia, seminars, or other meetings sponsored or co-sponsored by NASA.

- SPECIAL PUBLICATION. Scientific, technical, or historical information from NASA programs, projects, and missions, often concerned with subjects having substantial public interest.

- TECHNICAL TRANSLATION. English-language translations of foreign scientific and technical material pertinent to NASA's mission.

Specialized services that complement the STI Program Office's diverse offerings include creating custom thesauri, building customized databases, organizing and publishing research results ... even providing videos.

For more information about the NASA STI Program Office, see the following:

- Access the NASA STI Program Home Page at *http://www.sti.nasa.gov*

- E-mail your question via the Internet to help@sti.nasa.gov

- Fax your question to the NASA STI Help Desk at (301) 621–0134

- Phone the NASA STI Help Desk at (301) 621–0390

- Write to:
  NASA STI Help Desk
  NASA Center for AeroSpace Information
  7115 Standard Drive
  Hanover, MD 21076–1320

NASA/TM–2008–215342

# An Initial Investigation of the Effects of Turbulence Models on the Convergence of the RK/Implicit Scheme

*R. C. Swanson*
*Langley Research Center, Hampton, Virginia*

*C.-C. Rossow*
*DLR, Deutsches Zentrum für Luft- und Raumfahrt,*
*Institut für Aerodynamik und Strömungstechnik,*
*Braunschweig, Germany*

August 2008

# Acknowledgments

# Abstract

A three-stage Runge-Kutta (RK) scheme with multigrid and an implicit preconditioner has been shown to be an effective solver for the fluid dynamic equations. This scheme has been applied to both the compressible and essentially incompressible Reynolds-averaged Navier-Stokes (RANS) equations using the algebraic turbulence model of Baldwin and Lomax (BL). In this paper we focus on the convergence of the RK/implicit scheme when the effects of turbulence are represented by either the Spalart-Allmaras model or the Wilcox $k$-$\omega$ model, which are frequently used models in practical fluid dynamic applications. Convergence behavior of the scheme with these turbulence models and the BL model are directly compared. For this initial investigation we solve the flow equations and the partial differential equations of the turbulence models indirectly coupled. With this approach we examine the convergence behavior of each system. Both point and line symmetric Gauss-Seidel are considered for approximating the inverse of the implicit operator of the flow solver. To solve the turbulence equations we use a diagonally dominant alternating direction implicit (DDADI) scheme. Computational results are presented for three airfoil flow cases and comparisons are made with experimental data. We demonstrate that the two-dimensional RANS equations and transport-type equations for turbulence modeling can be efficiently solved with an indirectly coupled algorithm that uses the RK/implicit scheme for the flow equations.

# Contents

# 1 Introduction

Reliable and sufficient convergence for steady-state computations of turbulent flows continues to be a challenge in computational fluid dynamics. Here sufficient convergence means that the residuals of the fluid dynamic equations and the equation set of a turbulence model are reduced to a level below the truncation error of the numerical scheme. In many applications a turbulence model has one or more partial differential equations (PDEs) which have a transport form and represent the effects of turbulence on the flow. When solving the transport-type equations of turbulence models, either directly or indirectly coupled to the flow equations, the residuals are frequently reduced only two orders of magnitude. In addition, the poor convergence of these transport-type equations adversely effects the convergence of the flow equations. Of course, when adequate convergence is not achieved, there is no assurance that the results obtained represent an acceptable approximation of the solution even from an engineering perspective. Thus, there is a strong need for improved numerical methods for not only obtaining steady-state solutions but also unsteady solutions when using a dual time-stepping scheme.

When attempting to develop an improved numerical method for solving the Reynolds-averaged Navier-Stokes (RANS) equations a necessary consideration is the coupling of the RANS equations and the equation or equations of the turbulence model being applied. If both the fluid dynamic and turbulence equations are directly coupled, then the characterization of the discrete system can change. That is, with appropriate discretization the fluid dynamic equations are positive definite (sometimes called a vector positive system [1]), making them amenable to relaxation, but the directly coupled system may not be due to the equation set for the turbulence model [2]. The numerical stiffness of the entire system is also much higher due to the source terms of the turbulence model. An alternative is to use indirect coupling of the two equation sets. Generally, in an iterative solution process with this approach the flow variables are updated while the turbulence variables are frozen; and then, the turbulence variables are updated while the flow variables are treated as fixed quantities. By indirectly coupling the equations we can focus on the specific properties of each equation set to obtain the best possible convergence of the two systems of equations. Furthermore, we can identify the essential properties of an algorithm for efficiently solving the directly coupled system. There are common design criteria for the algorithms of both equation sets. These requirements are as follows: (1) high Courant-Friedrichs-Lewy (CFL) limit, (2) convergence with weak dependency on mesh density (e.g., computational effort approaching at least $O(N \log N)$), (3) suitable for stiff discrete systems. In addition, for the equation set of the turbulence model there must also be appropriate treatment of any source terms so that convergence is not adversely affected.

A candidate for the flow solver of the loosely coupled system is the RK/implicit scheme. Previously, Rossow [3] and Swanson et al. [4] demonstrated that fast convergence can be obtained for both the two-dimensional (2-D) and three dimensional (3-D) RANS equations with the RK/implicit scheme and multigrid when using the Baldwin-Lomax (BL) algebraic eddy viscosity model [5]. The underlying three-stage RK scheme of this algorithm is important for clustering of the eigenvalues associated with the error components of the iterative process. This makes the scheme amenable to Krylov subspace iterative methods, which can provide additional convergence acceleration. Preconditioning with a fully implicit operator allows a CFL number of 1000. The implicit operator can be approximately inverted with either point or line symmetric Gauss-Seidel (SGS).

The main purpose of this work is to initiate an effort to satisfy the need to significantly augment the effectiveness (as measured by reliability and efficiency) of algorithms for solving the RANS equations and the PDEs of turbulence models. In this preliminary effort we assess the performance of an efficient RANS solver (i.e., RK/implicit scheme) when the turbulent viscosity field is generated by solving transport-type equations. Three turbulence models are considered. One is the BL model, which is used as a reference model. The other two models are the Spalart-Allmaras (SA) and Wilcox $k$-$\omega$ models, which are transport-type equation models that are frequently used in solving a variety of fluid dynamics problems. In the first section of this paper we describe these two turbulence models indicating the specifics of their implementation. Then the numerical schemes for solving the flow and turbulence equations are presented and briefly discussed. For this initial work we use a diagonally dominant alternating direction implicit (DDADI) scheme to solve the equation sets of the turbulence models. A subiterative procedure is also used to reduce factorization error of the DDADI scheme. In the results section we investigate the convergence behavior of the RK/implicit scheme with multigrid when solving the RANS equations with the three different turbulence models. The convergence behavior of the scheme with the SA and $k$-$\omega$ models is compared with that of the BL model, which was used in the initial development of the numerical scheme.

## 2 Turbulence Models

The current implementation of the BL model is given in the paper by Swanson and Turkel [6]. In the first part of this section we present the Spalart-Allmaras model and discuss the particular form of the model used in this investigation. Then we describe the Wilcox $k$-$\omega$ model and delineate the specific assumptions associated with the form of the model that we have applied. A stress limiter (with parameter) for the specific dissipation rate is defined. In a subsequent section on results we discuss the effect of the stress-limiter parameter on the extent of flow separation.

### 2.1 Spalart-Allmaras Model

Here we provide a sufficient description of the SA model to allow implementation. A detail discussion explaining the modeling of the physical terms in the single transport-type equation is given in the paper by Spalart and Allmaras [7]. Let $\nu_t$ be the eddy viscosity, which is defined by

$$\nu_t = \tilde{\nu}\, f_{v1}, \qquad f_{v1} = \frac{\chi^3}{\chi^3 + C_{v1}^3}, \qquad \chi \equiv \frac{\tilde{\nu}}{\nu}, \tag{1}$$

where $\nu$ is the kinematic viscosity. The transport-type equation for $\tilde{\nu}$ given in [7] is written as

$$\frac{\partial \tilde{\nu}}{\partial t} + u_j \frac{\partial \tilde{\nu}}{\partial x_j} = C_{b1}(1 - f_{t2})\tilde{S}\tilde{\nu} + \frac{1}{\sigma}\left\{ \frac{\partial \tilde{\nu}}{\partial x_j}\left[(\nu + \tilde{\nu})\frac{\partial \tilde{\nu}}{\partial x_j}\right] + C_{b2}\frac{\partial \tilde{\nu}}{\partial x_j}\frac{\partial \tilde{\nu}}{\partial x_j} \right\}$$
$$- \left( C_{w1}f_w - \frac{C_{b1}}{\kappa^2}f_{t2} \right)\left(\frac{\tilde{\nu}}{d}\right)^2 + \mathcal{S}, \tag{2}$$

where $t$ is time, $x_j$ and $u_j$ are Cartesian coordinates and velocity components, respectively, and

$$\tilde{S} \equiv S + \frac{\tilde{\nu}}{\kappa^2 d^2}\, f_{v2}, \qquad f_{v2} = 1 - \frac{\chi}{1 + \chi f_{v1}}, \tag{3}$$

with $S$ being the magnitude of the vorticity ($|\mathbf{\Omega}|$), $d$ delineating the distance to the closest wall boundary, and $\kappa$ denoting the von Kármán constant. The first, second, and third terms on the right-hand side of Eq. 2 represent the production, diffusion, and destruction terms, respectively. The last term is a source term, which is defined by

$$\mathcal{S} = f_{t1}\,\Delta U^2, \tag{4}$$

where $\Delta U$ is the norm of the difference between the velocity at the transition location and that at a field point being considered. The function

$$f_w = g\left(\frac{1 + C_{w3}^6}{g^6 + C_{w3}^6}\right)^{1/6} \tag{5}$$

where

$$g = r + C_{w2}\left(r^6 - r\right), \qquad r \equiv \frac{\tilde{\nu}}{\tilde{S}\kappa^2 d^2}. \tag{6}$$

For large values of $r$ the function $f_w$ goes to a constant. Thus, it can be truncated to a value of 10. The function $f_{t2}$ is defined as

$$f_{t2} = C_{t3}\exp(-C_{t4}\chi^2) \tag{7}$$

Spalart includes the transition function given by

$$f_{t1} = C_{t1}\,g_t \exp\left[-C_{t2}\frac{\omega_t^2}{\Delta U^2}(d^2 + g_t^2 d_t^2)\right], \tag{8}$$

3

where $d_t$ is the distance from the field point to the boundary-layer trip (where trip refers to a known location for transition), $\omega_t$ is the wall vorticity at the trip,

$$g_t \equiv \min\left[0.1,\ \Delta U/(\omega_t \Delta x_t)\right]. \tag{9}$$

and $\Delta x_t$ is the grid spacing along the wall at the trip.

In the present implementation of the model we do not include the trip function, which is usually neglected when applying the model (e.g., Ref. [8]). In addition, for convenience, after some algebra and rearranging of terms, we rewrite Eq. 2 as

$$\frac{\partial \tilde{\nu}}{\partial t} + u_j \frac{\partial \tilde{\nu}}{\partial x_j} = C_{b1}(1 - f_{t2})|\mathbf{\Omega}|\tilde{\nu} + \left\{ C_{b1}[(1 - f_{t2})f_{v2} + f_{t2}]\kappa^{-2} - C_{w1}f_w \right\} \left( \frac{\tilde{\nu}}{d} \right)^2 \tag{10}$$
$$+ \frac{1}{\sigma} \frac{\partial}{\partial x_j} \left[ (\nu + (1 + C_{b2})\tilde{\nu}) \frac{\partial \tilde{\nu}}{\partial x_j} \right] - \frac{C_{b2}}{\sigma} \tilde{\nu} \frac{\partial^2 \tilde{\nu}}{\partial x_j^2}.$$

The constants of the model are as follows:

$$C_{b1} = 0.1355, \quad \sigma = \frac{2}{3}, \quad C_{b2} = 0.622, \quad \kappa = 0.41, \quad C_{w1} = \frac{C_{b1}}{\kappa} + \frac{1 + C_{b2}}{\sigma}, \tag{11}$$
$$C_{w2} = 0.3, \quad C_{w3} = 2, \quad C_{v1} = 7.1, \quad C_{t1} = 1, \quad C_{t2} = 2, \quad C_{t3} = 1.2, \quad C_{t4} = 0.5.$$

On a solid boundary $\tilde{\nu} = 0$. Originally, the free-stream $\tilde{\nu}$ was set to $1.342\,\nu_\infty$, where $\nu_\infty$ is the free-stream kinematic viscosity. In order to avoid the possibility of a delayed transition, the free-stream value of $\tilde{\nu}$ is set to $3\,\nu_\infty$, as suggested by Rumsey [9].

## 2.2  Wilcox $k$-$\omega$ Model

A detailed discussion of Wilcox $k$-$\omega$ model is given in the 3rd edition of the book on turbulence modeling by Wilcox [10]. Before writing the two transport equations of this model, we define certain quantities. In general, the mean-molecular-stress tensor $\bar{t}_{ij}$ and the Reynolds-stress tensor $\tau_{ij}$ are given by

$$\bar{t}_{ij} = 2\mu \bar{S}_{ij}, \qquad \bar{\rho}\tau_{ij} = 2\mu_t \bar{S}_{ij} - \frac{2}{3}\bar{\rho}k\delta_{ij}, \qquad \bar{S}_{ij} = S_{ij} - \frac{1}{3}\frac{\partial \tilde{u}_k}{\partial x_k}\delta_{ij}. \tag{12}$$

where $\rho$ is density, $\mu$ is the molecular viscosity, $\mu_t$ is the turbulent viscosity, $k$ is the turbulence kinetic energy, and $\delta_{ij}$ is the kronecker delta. The overbar and tilde indicate Reynolds-averaged and mass-averaged quantity, respectively. The mean-strain-rate tensor $S_{ij}$ in Eq. 12 and the mean-rotation tensor $\Omega_{ij}$ are defined as follows:

$$S_{ij} = \frac{1}{2}\left( \frac{\partial \tilde{u}_i}{\partial x_j} + \frac{\partial \tilde{u}_j}{\partial x_i} \right), \qquad \Omega_{ij} = \frac{1}{2}\left( \frac{\partial \tilde{u}_i}{\partial x_j} - \frac{\partial \tilde{u}_j}{\partial x_i} \right). \tag{13}$$

The turbulent viscosity is given by

$$\mu_t = \frac{\bar{\rho}k}{\omega}, \tag{14}$$

where $\omega$ is the specific dissipation rate. The equation for the turbulence kinetic energy can be written as

$$\frac{\partial}{\partial t}(\bar{\rho}k) + \frac{\partial}{\partial x_j}(\bar{\rho}\tilde{u}_j k) = \bar{\rho}\tau_{ij}\frac{\partial \tilde{u}_i}{\partial x_j} - \beta^* \bar{\rho}k\omega + \frac{\partial}{\partial x_j}\left[ \left( \mu + \sigma^* \frac{\bar{\rho}k}{\omega} \right) \frac{\partial k}{\partial x_j} \right]. \tag{15}$$

The equation for the specific dissipation rate is given by

$$\frac{\partial}{\partial t}(\bar{\rho}\omega) + \frac{\partial}{\partial x_j}(\bar{\rho}\tilde{u}_j\omega) = \alpha\frac{\omega}{k}\bar{\rho}\tau_{ij}\frac{\partial\tilde{u}_i}{\partial x_j} - \beta\bar{\rho}\omega^2 + \sigma_d\frac{\bar{\rho}}{\omega}\frac{\partial k}{\partial x_j}\frac{\partial\omega}{\partial x_j} \tag{16}$$

$$+ \frac{\partial}{\partial x_j}\left[\left(\mu + \sigma\frac{\bar{\rho}k}{\omega}\right)\frac{\partial\omega}{\partial x_j}\right].$$

The first, second, and last terms of the right-hand sides of Eqs. 15 and 16 are due to the production, destruction, and diffusion of turbulence, respectively. The third term in Eq. 16 is a cross-diffusion term. For the basic implementation of the $k$-$\omega$ model we use the the 1988 version [11], following the approach of Ref. [8]. This version uses the incompressible assumption, which means that the volumetric dilatation term in the total strain-rate tensor of Eq. 12 vanishes, and it does not include the cross-diffusion term. In addition, it neglects the term containing $k$ in the Reynolds-stress tensor, which is important for high Mach number flows, and it replaces the product of the mean-strain-rate tensor and velocity gradient in the turbulence production term by the square of the magnitude of the vorticity,

$$|\boldsymbol{\Omega}|^2 = 2\bar{\Omega}_{ij}\bar{\Omega}_{ij}, \tag{17}$$

where $\bar{\Omega}_{ij}$ is the zero trace of the mean rotation tensor. When we write $\bar{\Omega}_{ij}\bar{\Omega}_{ij}$, it means the scalar (or double dot) product of two tensors. Then Eqs. 15 and 16 are replaced by

$$\frac{\partial k}{\partial t} + \tilde{u}_j\frac{\partial k}{\partial x_j} = \frac{\mu_t}{\bar{\rho}}|\boldsymbol{\Omega}|^2 - \beta^*k\omega + \frac{1}{\bar{\rho}}\frac{\partial}{\partial x_j}\left[\left(\mu + \sigma^*\frac{\bar{\rho}k}{\omega}\right)\frac{\partial k}{\partial x_j}\right], \tag{18}$$

$$\frac{\partial\omega}{\partial t} + \tilde{u}_j\frac{\partial\omega}{\partial x_j} = \alpha\frac{\omega}{k}\frac{\mu_t}{\bar{\rho}}|\boldsymbol{\Omega}|^2 - \beta\omega^2 + \frac{1}{\bar{\rho}}\frac{\partial}{\partial x_j}\left[\left(\mu + \sigma\frac{\bar{\rho}k}{\omega}\right)\frac{\partial\omega}{\partial x_j}\right]. \tag{19}$$

The basic version of the $k$-$\omega$ model is modified by using key model changes according to Wilcox [12]. For additional details see Wilcox [10]. One modification is the introduction of a stress limiter in the definition of $\omega$. With this change the original $\omega$ appearing in Eqs. 14, 18, and 19 is replaced in the present form of the $k$-$\omega$ model by

$$\tilde{\omega} = \max\left\{\omega, \quad C_{lim}\sqrt{\frac{2\bar{\Omega}_{ij}\bar{\Omega}_{ij}}{\beta^*}}\right\}, \qquad C_{lim} = 0.95. \tag{20}$$

This change is quite important for separated flows. In particular, it reduces the magnitude of the eddy viscosity when the production of turbulence energy exceeds the dissipation rate, which allows larger separation bubbles (as demonstrated by Huang [13]). The remaining modifications in the model involve the closure coefficients.

The closure coefficients for the $k$-$\omega$ model are as follows:

$$\alpha = \frac{13}{25}, \quad \beta = \beta_o f_\beta, \quad \beta^* = \frac{9}{100}, \quad \sigma = \frac{1}{2}, \quad \sigma^* = \frac{1}{2}, \quad \sigma_{do} = \frac{1}{8}, \quad \beta_o = 0.0708, \tag{21}$$

$$Pr_t = \frac{8}{9}, \quad f_\beta = \frac{1 + 85\chi_\omega}{1 + 100\chi_\omega}, \quad \chi_\omega \equiv \left|\frac{\Omega_{ij}\Omega_{jk}\hat{S}_{ki}}{(\beta^*\omega)^3}\right|, \quad \hat{S}_{ki} = S_{ki} - \frac{1}{2}\frac{\partial\tilde{u}_m}{\partial x_m}\delta_{ki},$$

$$\sigma_d = \begin{cases} 0, & \frac{\partial k}{\partial x_j}\frac{\partial\omega}{\partial x_j} \le 0 \\[2mm] \sigma_{do}, & \frac{\partial k}{\partial x_j}\frac{\partial\omega}{\partial x_j} > 0 \end{cases}$$

where $Pr_t$ is the turbulent Prandtl number. The boundary conditions for the model are the following. On a solid wall boundary $k = k_w$, which is zero, and $\omega$ is determined by

$$\omega = \omega_w = \frac{60\mu_1}{\rho_1\beta(d_1)^2}, \tag{22}$$

5

where $\rho_1$ and $\mu_1$ are the values of density and molecular viscosity at the center of the mesh cell adjacent to the wall. In the free-stream

$$k = k_\infty = 9 \times 10^{-9} \, u_\infty^2, \quad \omega = \omega_\infty = 1 \times 10^{-6} \left( \frac{u_\infty^2}{\nu_\infty} \right). \tag{23}$$

In general, an important consideration when applying turbulence models is the effect of initialization on the numerical solution process. For example, when initializing a computation with free-stream conditions, numerical difficulties (e.g., convergence stall or even divergence of the iterative procedure for steady-state solutions) can occur in regions where $\omega$ becomes small, which allows disturbances in the strain rate to result in large values of the turbulent viscosity. Menter [14] considers a transport-type equation for the eddy viscosity $\nu_t$ to show that the production term becomes very large when $\omega$ goes to zero and $\nu_t$ is finite. In order to prevent this from occurring, especially during the initial stages of a calculation, Menter suggests applying a constraint on the production term. Let $P_k$ and $D_k$ denote the production and destruction contributions, respectively, in Eq. 20. Then, according to Menter a suitable limiter on the turbulence production is given by

$$\tilde{P}_k = min(P_k, \, 20D_k). \tag{24}$$

We have found that this limiter works well in turbulent airfoil flow applications.

# 3 Numerical Schemes

To solve the RANS equations we use the RK/implicit scheme. Complete details of the scheme are presented in the papers of Rossow [3] and Swanson et al. [4]. The SA and $k$-$\omega$ turbulence models require the solution of one and two transport-type equations, respectively. In the present work we do not directly couple the solution of the fluid dynamic equations with the additional equation or equations of the turbulence models. To solve the transport-type equations of the SA and $k$-$\omega$ turbulence models we use a DDADI scheme. In the first part of this section we present the essential elements of the RK/implicit scheme. Then we describe the DDADI scheme.

## 3.1 RK/Implicit Scheme

We apply a finite-volume approach to discretize the fluid dynamic equations and use the approximate Riemann solver of Roe [15] to obtain a second-order discretization of the advection terms. The viscous terms are discretized with a second-order central difference approximation. To obtain an explicit update to the solution vector for the flow equations we use a three-stage RK scheme. The update for the $q$-th stage of a RK scheme is given by

$$\mathbf{W}^{(q)} = \mathbf{W}^{(0)} + \delta \mathbf{W}^{(q)}, \tag{25}$$

where the change in the solution vector $\mathbf{W}$ is

$$\delta \mathbf{W}^{(q)} = \mathbf{W}^{(q)} - \mathbf{W}^{(0)} = -\alpha_q \frac{\Delta t}{\mathcal{V}} \mathcal{L} \, \mathbf{W}^{(q-1)}, \tag{26}$$

and $\mathcal{L}$ is the complete difference operator for the system of equations. Here $\alpha_q$ is the RK coefficient of the $q$-th stage, $\Delta t$ is the time step, and $\mathcal{V}$ is the volume of the mesh cell being considered. To extend the support of the difference scheme we consider implicit residual smoothing. Applying the smoothing technique of Ref. [16] we have the following:

$$\mathcal{L}_i \, \overline{\delta \mathbf{W}}^{(q)} = \delta \mathbf{W}^{(q)}, \tag{27}$$

where $\mathcal{L}_i$ is an implicit operator. By approximately inverting the operator $\mathcal{L}_i$ we obtain

$$\overline{\delta \mathbf{W}}^{(q)} = -\alpha_q \frac{\Delta t}{\mathcal{V}} \mathcal{P} \, \mathcal{L} \, \mathbf{W}^{(q-1)} = -\alpha_q \frac{\Delta t}{\mathcal{V}} \mathcal{P} \sum_{\text{all faces}} \mathbf{F}_n^{(q-1)} \, S, \tag{28}$$

6

where $\mathcal{P}$ is a preconditioner defined by the approximate inverse $\widetilde{\mathcal{L}}_i^{-1}$, $\mathbf{F}_n$ is the normal flux density vector at the cell face, and $S$ is the area of the cell face. The change $\overline{\delta\mathbf{W}}^{(q)}$ replaces the explicit update appearing in Eq. (25). Thus, each stage in the RK scheme is preconditioned by an implicit operator.

A first order upwind approximation based on the Roe scheme is used for the convection derivatives in the implicit operator. To derive this operator one treats the spatial discretization terms in the flow equations implicitly and applies linearization. For a detailed derivation see Rossow [3]. Substituting for the implicit operator in Eq. (27), we obtain for the $q$-th stage of the RK scheme

$$\left[ I + \varepsilon \frac{\Delta t}{\mathcal{V}} \sum_{\text{all faces}} \mathbf{A}_n S \right] \overline{\delta\mathbf{W}}^{(q)} = -\alpha_q \frac{\Delta t}{\mathcal{V}} \sum_{\text{all faces}} \mathbf{F}_n^{(q-1)} S = \widehat{\mathbf{R}}^{(q-1)}, \tag{29}$$

where the matrix $\mathbf{A}_n$ is the flux Jacobian associated with $\mathbf{F}_n$ at a cell face, $\widehat{\mathbf{R}}^{(q-1)}$ represents the residual function for the $(q-1)$-th stage, and $\varepsilon$ is an implicit parameter. The parameter $\varepsilon$ is taken to be 0.7. Analysis and discussion concerning choosing $\varepsilon$ is given in Swanson et al. [4]. The matrix $\mathbf{A}_n$ can be decomposed into $\mathbf{A}_n^+$ and $\mathbf{A}_n^-$, which are associated with the positive and negative eigenvalues of $A_n$ and defined by

$$\mathbf{A}_n^+ = \frac{1}{2}\left(\mathbf{A}_n + |\mathbf{A}_n|\right), \quad \mathbf{A}_n^- = \frac{1}{2}\left(\mathbf{A}_n - |\mathbf{A}_n|\right). \tag{30}$$

If we substitute for $\mathbf{A}_n$ in Eq. (29) using the definitions of Eq. (30), then the implicit scheme can be written as

$$\left[ I + \varepsilon \frac{\Delta t}{\mathcal{V}} \sum_{\text{all faces}} \mathbf{A}_n^+ S \right] \overline{\delta\mathbf{W}}_{i,j}^{(q)} = \widehat{\mathbf{R}}_{i,j}^{(q-1)} - \varepsilon \frac{\Delta t}{\mathcal{V}} \sum_{\text{all faces}} \mathbf{A}_n^- \overline{\delta\mathbf{W}}_{NB}^{(q)} S, \tag{31}$$

where the indices $(i,j)$ indicate the cell of interest, and $NB$ refers to all the direct neighbors of the cell being considered. Consider traversing the boundary of a mesh cell in a counterclockwise manner, with the positive surface normal vector always pointing outward from the cell. Then, as discussed by Rossow [17], the quantity $\mathbf{A}_n^- \overline{\delta\mathbf{W}}$ represents the flux density change associated with waves having a negative wave speed (i.e., waves that enter the cell $(i,j)$ from outside). Only the neighbor cells $NB$ can contribute to these changes in flux density. Similarly, the quantity $\mathbf{A}_n^+ \overline{\delta\mathbf{W}}$ represents flux density changes associated with positive wave speeds (i.e., waves that leave the cell $(i,j)$). These flux density changes are determined only by information from within the cell $(i,j)$.

To solve Eq. (31) for the changes in conservative variables $\overline{\delta\mathbf{W}}_{i,j}^{(q)}$, the $4 \times 4$ matrix on the left-hand side of Eq. (31) must be inverted. It is sufficient to approximate the inverse of the implicit operator. An adequate approximate inverse is obtained with two symmetric Gauss-Seidel sweeps. To initialize the iterative process the unknowns are set to zero.

We consider two approaches for approximating the inverse of the implicit operator. One method is to apply two sweeps of point symmetric Gauss-Seidel (SGS) relaxation. The other is to apply radial line (or j-line) SGS sweeps. We should point out that when referring to this type of SGS in the text the modifiers line and j-line are used interchangeably. When computing boundary layer and free shear-layer turbulent flows the computational grid is usually strongly clustered to adequately resolve the steep flow-field gradients, which produces a strong grid anisotropy and a high degree of stiffness in the discrete flow equations. Line solvers are frequently employed with structured grid solvers in the direction of strongest coupling to relieve the stiffness associated with the grid anisotropy. Even on unstructured grids line solvers can be applied. By constructing artificial lines in an unstructured grid that extend only through the regions of strongest coupling, Mavriplis [18] has demonstrated effective reduction of the numerical stiffness.

With line SGS we apply the implicit operator across the wake line (the line emanating from the trailing edge of an airfoil), which we call a fully implicit treatment. It is also possible to lag the boundary condition at the wake line rather than extending the line solve across the wake line. This approach can also work well provided local relaxation or subiterations are performed to compensate for the lagging of the wake boundary condition. Although this may be a more convenient option, from the implementation point of view, for multiblock structured grid methods, we use the fully implicit method in this paper to obtain a measure of the best possible convergence

with the line SGS relaxation as the smoother for the multigrid method. Furthermore, a variation on this wake treatment can be applied with unstructured grid methods by appropriate ordering of the unknowns.

Due to the upwind approximation used for the implicit operator, the coefficients for the RK scheme are also based on an upwind scheme. For computational efficiency we apply a three-stage RK scheme with the coefficients

$$[\alpha_1, \alpha_2, \alpha_3] = [0.15, \ 0.4, \ 1.0]$$

from Ref. [19]. In the application of the three-stage RK/implicit scheme as the smoother of a full approximation storage (FAS) multigrid method, the CFL number is increased to 1000 after 10 multigrid cycles. During the first 10 cycles the CFL is 16. A W-type cycle is used to execute the multigrid. Details of the multigrid method are given in the paper by Swanson et al. [4].

## 3.2  DDADI Scheme

For simplicity we describe the DDADI scheme from the perspective of the SA equation. After discretizing Eq. 10, we consider the implicit form

$$(I + L_x + L_y + \bar{\mathcal{S}}) \, \Delta \tilde{\nu} = -\bar{R} \tag{32}$$

where $L_x$ and $L_y$ are the linear discrete operators for the terms of the transport-type equation, $\bar{\mathcal{S}}$ is the source term containing the production and destruction of turbulence contributions, and $\bar{R}$ is the residual function. The operators for the two coordinate directions are as follows:

$$L_x = \frac{\Delta t}{\mathcal{V}} \, \theta \left[ \delta_x^u - (\delta_x \beta_1 + \beta_2 \delta_x) \delta_x \right], \quad L_y = \frac{\Delta t}{\mathcal{V}} \, \theta \left[ \delta_y^u - (\delta_y \beta_1 + \beta_2 \delta_y) \delta_y \right], \tag{33}$$

where $\delta^u$ is a first-order upwind operator for the convection term, $\delta$ is a standard central difference operator, and the coefficients $\beta_1$, $\beta_2$ are defined by the diffusion term of the turbulence model. The parameter $\theta$ indicates the temporal accuracy. If $\theta = 1/2$, then the time derivative is approximated by a central difference, which is second-order accurate (i.e., Crank-Nicolson scheme). When $\theta = 1$ the approximation is a first-order backward difference, and we have a fully (an Euler) implicit scheme. The parameter $\theta$ may also be viewed as a measure of implicitness with $0 < \theta < 1$ and $\theta > 1$ indicating under-relaxation and over-relaxation, respectively. The source term and the residual function are defined by

$$\bar{\mathcal{S}} = \frac{\Delta t}{\mathcal{V}} \, \theta \mathcal{S}, \quad \bar{R} = \frac{\Delta t}{\mathcal{V}} R. \tag{34}$$

For the advection and diffusion terms of the residual function we use first-order upwind difference and central difference approximations, respectively. A first-order approximation of advection terms is frequently applied in the implementation of turbulence models in order to promote positivity of the turbulence variables. In general, this is not sufficient to ensure positivity, so usually there is also limiting (clipping) of the turbulence quantities and/or certain terms (e.g., production term) in the set of turbulence field equations.

An appropriate linearization of the source term is extremely important to allow the use of large CFL numbers. One approach for solving Eq. 32 is to factor the implicit (left-hand side) operator and apply the DDADI scheme. Define the diagonal contribution in Eq. 32 as

$$D = I + D_x + D_y + \bar{\mathcal{S}}, \tag{35}$$

where $D_x$ and $D_y$ are the diagonal parts of $L_x$ and $L_y$, respectively. Then, after factoring out $D$, we factor the resulting operator, obtaining

$$D \left[ I + D^{-1}(L_y - D_y) \right] \left[ I + D^{-1}(L_x - D_x) \right] \Delta \tilde{\nu} = -\bar{R}. \tag{36}$$

The next step is to factor $D^{-1}$ from each term enclosed by brackets, which gives

$$\left[ I + L_y + D_x + \bar{\mathcal{S}} \right] D^{-1} \left[ I + L_x + D_y + \bar{\mathcal{S}} \right] \Delta \tilde{\nu} = -\bar{R} \tag{37}$$

8

To invert this implicit operator, we solve iteratively the one-dimensional systems

$$\left[ I + L_y + D_x + \bar{S} \right] q_1 = -\bar{R}, \tag{38}$$
$$\left[ I + L_x + D_y + \bar{S} \right] q_2 = D\, q_1,$$

where $q_2 = \Delta\tilde{\nu}$ and

$$\tilde{\nu}^{n+1} = \tilde{\nu}^n + \Delta\tilde{\nu}. \tag{39}$$

In order to prevent deterioration in the allowable CFL number and damping behavior of the DDADI scheme due to the factorization error and possible boundary condition lagging error, we use subiteration. Following Klopfer et al. [20] the subiterative process can be written as

$$\left[ I + L_y + D_x + \bar{S} \right] \Delta q_1 = D(q_2^m - q_1^m), \tag{40}$$
$$\left[ I + L_x + D_y + \bar{S} \right] \Delta q_2 = D(q_1^{m+1} - q_2^m).$$

where

$$\Delta q_k = q_k^{m+1} - q_k^m,\ k = 1,\, 2;\ m \geq 1, \qquad q_2^m = \Delta\tilde{\nu}^m \tag{41}$$

with $m$ denoting the subiteration index. Convergence with iteration and subiteration, Eqs. 38 and 40, can be further accelerated by choosing an appropriate implicit parameter $\theta$, just as we do for the fluid dynamic equations.

The unknown $\tilde{\nu}$ appears in the denominator of some of the contributions to the source term of the SA model. Since the unknown vanishes at the wall, it can happen during the iterative process that at the first point off the wall the $\tilde{\nu}$ becomes zero. This possibility can easily be prevented in the usual way (i.e., take maximum of unknown and a very small number).

For the SA model, four iterations and one subiteration of the DDADI scheme are performed on each stage of the RK scheme when on the fine grid of each multigrid cycle for the flow equations. After 15 multigrid cycles the number of iterations is reduced to two. In evaluating the fine-grid residuals of the flow equations for restriction, we also update the turbulent viscosity. The additional work required for a subiteration is significantly less than for an iteration because the implicit coefficients do not have to be recomputed. There is only about a 1% increase in computational time per iteration for a subiteration

As indicated previously, the DDADI scheme just described is also used to solve the two equations of the $k$-$\omega$ model. When solving these equations we experience difficulties in simply using a CFL number of 1000 from the beginning of the iterative process, as we do when solving the SA model equation. Instead, we increase the CFL number from 20 to 1000 over the first 3 multigrid cycles in advancing the solution of the flow equations. For each stage of the RK scheme five iterations and one subiteration are performed with the DDADI scheme.

A desirable property for an effective implicit solver of PDEs is unconditional stability. This property is especially important for stiff equations. A linear analysis of an algorithm for solving a discrete system can often provide valuable insight into its stability and damping characteristics. MacCormack and Pulliam [21] investigated the characteristics of the modified approximate factorization (MAFk) scheme, with "k" subiterations per time step, by applying Fourier analysis to the Euler equations. The MAF1 scheme is equivalent to the DDADI scheme introduced by Bardina and Lombard [22]. Their analysis shows that when $\theta = 1$ the MAF1 scheme is conditionally stable. For high CFL numbers instability occurs for small wave number (long wavelength) modes. By increasing $\theta$ to 2, MacCormack and Pulliam also show that the DDADI scheme with a single subiteration is unconditionally stable. We have observed some different characteristics when solving the PDEs of the SA and $k$-$\omega$ turbulence models. In particular, based upon numerical experiments in solving these equations for airfoil applications we have demonstrated that the DDADI scheme with one subiteration and $\theta = 1$ is stable for high CFL numbers. With $\theta = 2$, we need two additional subiterations to maintain stability.

Figure 1 shows the effect of $\theta$ on the convergence of the DDADI scheme when applying the SA model in a transonic airfoil flow computation. Multigrid cycles are used on the horizontal axis for convenience in comparing
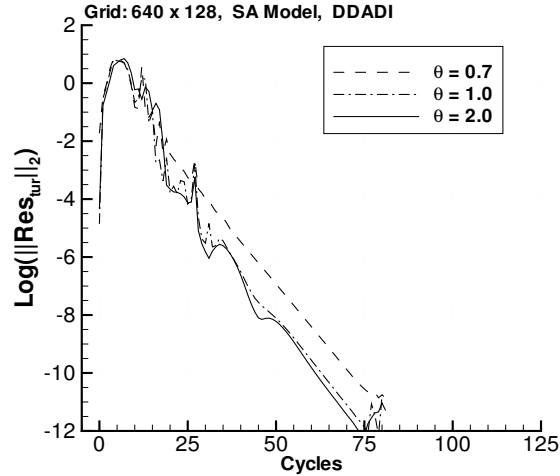
Figure 1: Effect of $\theta$ on the convergence of the DDADI scheme when solving the SA equation (grid: $640 \times 128$).

convergence of the flow equations with that of the turbulence equation. For these results the solution to the SA equation was updated on each of the three stages of the RK scheme used to solve the flow equations. With each update 4 iterations and 3 subiterations per iteration of the DDADI scheme were performed. As revealed in the figure, the asymptotic convergence rates are about the same for the three values of $\theta$ being considered. Although the residual is reduced slightly more when $\theta = 1$ and $\theta = 2$, the convergence history for $\theta = 0.7$ exhibits a monotonic behavior after the initial iterations. Thus, we generally choose $\theta = 0.7$.

When solving the PDEs of the turbulence models along the lines normal to the wake cut line, there are two distinct possibilities. One is to treat the wake implicitly, which means to solve for all the unknowns of a model along a given radial line in the wake; and thus, no boundary condition is imposed at the wake line. Venkatakrishnan [23] stresses the importance of the fully implicit approach. As indicated previously, an alternative approach is to lag the boundary condition at the wake cut line. In general, this method will slow down convergence; however, subiteration can be used to eliminate the boundary condition lagging error and convergence slowdown. Here again, in the interest of obtaining an estimate of the best convergence, we apply the implicit wake treatment.

The actual convergence of the DDADI scheme is not independent of the convergence of the flow solver. During the course of this investigation we have observed the following convergence behavior. Walsh and Pulliam [24] have also reported similar observations. The rate of development of the turbulence field can signficantly affect the convergence of the flow solver. Conversely, how well the flow solver converges can have an impact on the effectiveness of the scheme for solving the equation set of the turbulence model. Moreover, when the RANS and turbulence equations are being solved in a loosely coupled manner, an essential requirement for an effective total algorithm is that the numerical solution vector of each equation set exhibits a similar evolution rate. Since the present algorithm includes an effective flow solver, we have provided an amenable setting for the DDADI scheme and the overall algorithm.

## 4 Computational Results

A series of computations for turbulent, viscous flow over the RAE 2822 airfoil were performed to evaluate the convergence behavior of the RK/implicit scheme when applying the BL, SA, and $k$-$\omega$ turbulence models. In solving the RANS equations we used structured meshes with a C-type topology. We considered two mesh densities, one with 320 cells around the airfoil (256 cells on the airfoil) and 64 cells in the normal direction, and the other with twice as many cells in each coordinate direction. For the $640 \times 128$ grid the normal mesh spacing at the surface is approximately $6 \times 10^{-6}$, and the maximum surface cell aspect ratio is about 2000. The airfoil solu-

Table 1: Flow conditions for RAE 2822 airfoil.

| Cases | $M_\infty$ | $\alpha$ (deg.) | $Re_c$ | $x_{tr}/c$ |
|---------|-------|------|---------------------|------|
| Case 1  | 0.676 | 1.93 | $5.7 \times 10^6$ | 0.11 |
| Case 9  | 0.730 | 2.79 | $6.5 \times 10^6$ | 0.03 |
| Case 10 | 0.750 | 2.81 | $6.2 \times 10^6$ | 0.03 |

tions were calculated with the Case 1, Case 9 and Case 10 flow conditions (see Table 1) from the experimental investigation of Cook, McDonald and Firmin [25]. For Case 1 the flow is primarily subsonic with a relatively small region of supersonic flow. The other two cases are transonic. In Case 9 there is a fairly strong shock wave occurring on the upper surface of the airfoil, where as in Case 10 there is a sufficiently strong shock on the upper surface to cause significant flow separation behind the shock.

In all the applications the same boundary conditions were imposed for the fluid dynamic equations. On the surface the no-slip condition was applied. At the outer boundary Riemann invariants were used. A far-field vortex effect was included to specify the velocity for an inflow condition at the outer boundary. A detailed discussion of the boundary conditions is given in Ref. [6]. The calculations were started on the solution grid with the initial solution given as the free-stream conditions. When a full multigrid process was applied, the initial solution on a given level of refinement was obtained from a coarser level.

When solving the fluid dynamic equations with the RK/implicit scheme both point and line SGS were considered to approximate the inverse of the implicit operator. With the multigrid method four grid levels were used. Unless indicated otherwise, full multigrid (FMG) was not applied when solving the flow equations, making a more demanding challenge for the initial part of the iterative process. All computations were performed on a Dell XPS 630 computer, which has two quad-core processors at 2.66 GHz.

## 4.1   Point Symmetric Gauss-Seidel

In this section we investigate the convergence behavior of the RK/implicit scheme with point SGS(2), where the 2 refers to the number of symmetric sweeps, for approximating the inverse of the implicit operator. We also examine the effect of limiting the aspect ratio of the mesh cells in the wake of the airfoil flow. The $L_2$ norm of the residual of the continuity equation is used as a measure of convergence for the flow equations. For these results the calculations were terminated after either 125 multigrid cycles or a 13 orders of magnitude reduction in the residual.

We first consider the convergence of the flow equations with the RK/implicit scheme when applying the BL model. Figure 2 shows convergence histories of the residual and lift coefficient ($C_L$) for Case 1 on both the $320 \times 64$ and $640 \times 128$ grids. On the $320 \times 64$ grid the scheme converges at a rate of 0.714. There is a some slowdown in convergence on the $640 \times 128$, where the rate is 0.742. With the turbulent viscosity field produced by the BL model there is clearly no reduction in the asymptotic convergence rate (i.e., rate beyond approximately 8 orders of magnitude reduction in the residual) on a given grid. As we will see next, the turbulent viscosity fields generated with the other turbulence models do cause a slower asymptotic convergence rate when using point SGS(2).

Figure 3 shows the convergence of the solvers of the flow equations and the SA transport-type equation for Case 1 on the $320 \times 64$ grid. The CFL number for both the flow equations and the turbulence equation was 1000. As seen in Figure 3(a), there is significant slowdown in convergence after about 40 multigrid cycles (residual reduced 8 orders) in the absence of no limiting of the mesh cell aspect ratio (AR) in the wake. By limiting the wake aspect ratio to 1000 the residual is reduced two additional orders before a slowdown occurs. In the limiting the normal grid spacing in the airfoil wake is allowed to increase with distance downstream of the airfoil trailing edge. With an AR limit of 100 there is no deterioration in the asymptotic convergence rate. The convergence of the residual of the SA equation, which is displayed in Figure 3(b), responds in a similar way to the AR limiting.

Figure 4 shows the convergence histories on the $320 \times 64$ grid when applying the $k$-$\omega$ turbulence model. For
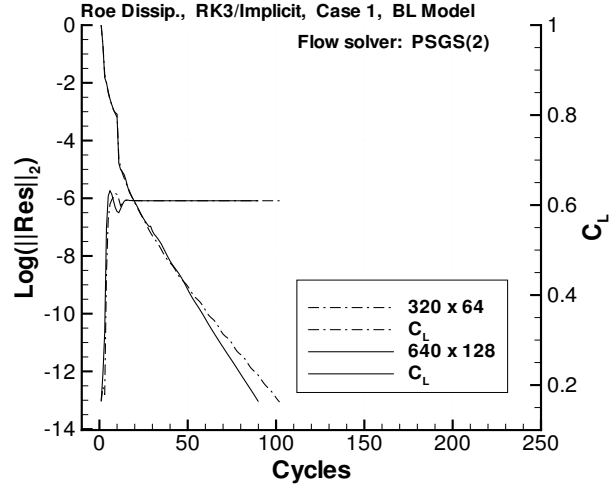
Figure 2: Convergence histories of Case 1 using point SGS with RK/implicit scheme and the BL model (grids: $320 \times 64$, $640 \times 128$).

the flow equations we again observe the slower asymptotic convergence rate when using the point SGS(2) scheme in the multigrid smoother. This slowdown is eliminated for both the flow and turbulence equations by limiting the wake AR to 1000. These results also seem to indicate that the $k$-$\omega$ model is less sensitive than the SA model to AR in the wake.

Clearly, for the two models the residual has been reduced well below the truncation error of the numerical discretization before the slower residual reduction rate occurs. This means that we have achieved converged solutions well before the onset of slowdown, and that further reduction in the residual does not improve the solutions. However, in more complex flow problems the source of this slowdown may prevent convergence. For this reason it is important to understand the cause of the slower asymptotic rate of convergence.

We now address the issue of why there is a slowdown in the asymptotic convergence rate when applying either the SA or the $k$-$\omega$ models and using point SGS for inverting the implicit operator in the RK/implicit scheme. Since there is no apparent slowdown indicated by the asymptotic convergence rate when the BL model and point SGS are employed, the mesh AR in the wake does not appear to be the primary source of the slower asymptotic rate when applying the SA and $k$-$\omega$ models. Another possible cause of the reduction in convergence rate is the difference in the turbulent viscosity fields in the wake. Thus, we consider a characterization of turbulent viscosity for all the turbulence models in the airfoil wake.

An important factor for the different turbulence models is how well they represent the physics of the airfoil near wake flow. The manner in which the models behave in the near wake can also significantly effect the convergence behavior of both the fluid dynamic and turbulence equations. Here the issue is not only the magnitude of the turbulent viscosity ($\mu_t$) but also how it varies as the flow proceeds from a wall-bounded shear layer to a free shear layer. In Figs. 5(a) - Figs. 5(c) we present the $\mu_t$ contours in the near wake region from solutions on the $320 \times 64$ grid obtained with the three turbulence models. The $\mu_t$ is scaled by the free-stream molecular viscosity ($\mu_\infty$). These results indicate that in the near wake the streamwise extent of higher levels of $\mu_t$ is much greater for the SA and $k$-$\omega$ models than for the BL model. Also, with the $k$-$\omega$ model, we observe unexpected rapid initial spreading of the $\mu_t$ field in the initial wake, resulting in a much greater lateral extent. Figure 5(d) shows that mesh refinement ($640 \times 128$ grid) produces a significant reduction of the $\mu_t$ field in the transverse direction, suggesting that resolution plays a key role in the development of the near wake flow. Some further discussion of the initial wake behavior is given in the Appendix. Turbulent viscosity profiles at four streamwise wake locations are displayed for each of the turbulence models in Fig. 6. For the BL model the peak value of $\mu_t$ occurs at the trailing edge, and a minimum value occurs at approximately the two chord location. From the complete turbulent

Table 2: Computational performance for Case 1 using different turbulence models. LSGS(2) used in solving flow equations and DDADI used to solve turbulence equations.

| Model | Grid | CPU Time (sec.) | MG Cycles | Convergence Rate |
|-------|------|-----------------|-----------|------------------|
| BL | $320 \times 64$ | 79 | 79 | 0.683 |
| SA | $320 \times 64$ | 100 | 79 | 0.684 |
| $k$-$\omega$ | $320 \times 64$ | 125 | 80 | 0.686 |
| | | | | |
| BL | $640 \times 128$ | 365 | 87 | 0.709 |
| SA | $640 \times 128$ | 544 | 87 | 0.708 |
| $k$-$\omega$ | $640 \times 128$ | 673 | 88 | 0.710 |

viscosity field we observe that a maximum $\mu_t$ value of about 400 persists into the far field. In contrast, both the SA and $k$-$\omega$ models have their peak value of $\mu_t$ occurring at around the two chord location, and then the peak $\mu_t$ decreases as the flow proceeds downstream. The maximum $\mu_t$ of these two models is roughly twice as large as that of the BL model. Figure 6 also shows that the $\mu_t$ values in the vicinity of the $y/c = 0$ line (i.e., the wake cut) are much higher for the SA and $k$-$\omega$ models than for the BL model. These higher levels of $\mu_t$ result in a much stronger coupling of the discrete equations through the diffusion terms. In addition, there is an augmentation in the influence of the source terms in the turbulence models. Both of these factors contribute to the increased need for implicit treatment across the cut line of the wake.

## 4.2   Line Symmetric Gauss-Seidel

In the next set of results we show the benefit of using j-line symmetric Gauss-Seidel (LSGS) to approximate the inverse of the implicit operator in the RK/implicit smoother. Figure 7 compares the convergence histories of the flow equations for Case 1 on the two grids when applying the three different turbulence models. With each model nearly the same convergence rate is obtained on $320 \times 64$ grid. Moreover, almost the same rate is attained for each model on the $640 \times 128$ grid. The convergence rates are given in Table 2. Figure 8 displays the convergence plots for the SA and $k$-$\omega$ models. For both of these models there is some slowdown in the convergence rate due to mesh refinement. In general, slower rates are expected since there is no component in the algorithm for the turbulence equations, such as multigrid, to reduce this effect. We need to keep in mind that if multigrid is introduced the emphasis is placed on the role of the scheme as a high-frequency smoother rather than a solver. As indicated in the papers by MacCormack and Pulliam [21] and Pulliam et al. [26], the DDADI scheme with subiteration has potential as an effective smoother.

The surface pressure and skin-friction distributions computed with the three turbulence models for Case 1 are compared in Figs. 9 and 10. The surface pressures are quite similar and exhibit good agreement with the data. The skin-friction coefficient $C_f$ is the wall shear stress divided by the dynamic pressure based on boundary-layer edge values. In Table 3 we give the computed lift and drag coefficients using the three models.

For Case 9 the convergence plots for the flow and turbulence equations are presented in Figs. 11 and 12. In this transonic case we observe somewhat similar convergence histories for the BL and SA turbulence models on both meshes. The convergence rate with these models is about 0.7 (see Table 4). With the $k$-$\omega$ model the convergence behavior is similar to that of the other two models on the $320 \times 64$ grid, but there is a brief slowdown in the convergence at around 30 cycles on the $640 \times 128$ grid. However, there is a fairly quick recovery in the convergence, and the asymptotic rate is similar to that of the other two models. This slowdown appears to be a consequence of the stress limiter of the model, which will be confirmed later. The convergence plots for the SA model are shown in Fig. 12(a). On the two grids the convergence rates are roughly the same after 40 cycles for the flow equations, but then there is an unexpected more rapid residual reduction on the finer grid. In addition, we do not see the oscillatory behavior that occurs for Case 1. For the $k$-$\omega$ model the convergence rates on the two grids are about the same. Although we do not observe a slower convergence with mesh refinement, one should

Table 3: Computed lift and drag coefficients for RAE 2822 airfoil. Numerical dissipation from Roe scheme. Weak grid clustering in neighborhood of shock wave.

| Cases | Model | Grid | $C_L$ | $C_D$ | $(C_D)_p$ | $(C_D)_v$ |
|-------|-------|------|-------|-------|-----------|-----------|
| Case 1 | BL | $320 \times 64$ | 0.6096 | 0.008280 | 0.002490 | 0.005790 |
| Case 1 | BL | $640 \times 128$ | 0.6096 | 0.008182 | 0.002380 | 0.005802 |
| Case 1 | SA | $320 \times 64$ | 0.5913 | 0.008458 | 0.002617 | 0.005841 |
| Case 1 | SA | $640 \times 128$ | 0.5902 | 0.008272 | 0.002486 | 0.005785 |
| Case 1 | $k$-$\omega$ | $320 \times 64$ | 0.6027 | 0.008183 | 0.002410 | 0.005773 |
| Case 1 | $k$-$\omega$ | $640 \times 128$ | 0.5933 | 0.008188 | 0.002400 | 0.005788 |
| | | | | | | |
| Case 9 | BL | $320 \times 64$ | 0.8541 | 0.01783 | 0.01230 | 0.005531 |
| Case 9 | BL | $640 \times 128$ | 0.8613 | 0.01804 | 0.01246 | 0.005585 |
| Case 9 | SA | $320 \times 64$ | 0.8186 | 0.01671 | 0.01118 | 0.005537 |
| Case 9 | SA | $640 \times 128$ | 0.8220 | 0.01662 | 0.01111 | 0.005507 |
| Case 9 | $k$-$\omega$ | $320 \times 64$ | 0.8333 | 0.01702 | 0.01155 | 0.005477 |
| Case 9 | $k$-$\omega$ | $640 \times 128$ | 0.8178 | 0.01644 | 0.01090 | 0.005545 |
| | | | | | | |
| Case 10 | BL | $320 \times 64$ | 0.8523 | 0.02910 | 0.02366 | 0.005435 |
| Case 10 | BL | $640 \times 128$ | 0.8781 | 0.03067 | 0.02512 | 0.005553 |
| Case 10 | SA | $320 \times 64$ | 0.7775 | 0.02584 | 0.02052 | 0.005317 |
| Case 10 | SA | $640 \times 128$ | 0.7850 | 0.02598 | 0.02069 | 0.005290 |
| Case 10 | $k$-$\omega$ | $320 \times 64$ | 0.7848 | 0.02581 | 0.02056 | 0.005256 |
| Case 10 | $k$-$\omega$ | $640 \times 128$ | 0.7672 | 0.02484 | 0.01951 | 0.005331 |

anticipate that on finer meshes a convergence slowdown will occur. Again this effect can possibly be limited by introducing multigrid into the algorithm for the turbulence equations. Furthermore, with the multigrid it may be possible to reduce the number of applications per RK stage of the DDADI scheme or whatever solver is being used for the PDEs of the turbulence models. In Figs. 13 and 14 we present the computed surface pressure and skin-friction distributions. The primary differences in the results with the three models is in the vicinity of the upper surface shock. For the SA and $k$-$\omega$ models the surface pressures are nearly the same. The variation in surface skin-friction is also quite similar, with the largest differences occurring in the region downstream of the shock. With the BL model the shock location is farther downstream, resulting in higher lift and drag coefficients (see Table 3).

The final set of results is for Case 10. In Figs. 15 and 16 the convergence plots for the flow and turbulence equations are presented. This transonic case is more difficult due to the stronger shock, which induces flow separation. The flow solver converges faster (rate of 0.72 on the $640 \times 128$ grid) when using the SA model. With the BL model the asymptotic convergence rate is slower. A comparison of the convergence rates is given in Table 5. From the convergence plots for the SA model, which are displayed in Fig. 16(a), we see that the residuals are reduced at least 9 orders of magnitude, and the rate of convergence on the $640 \times 128$ grid is somewhat faster. For the $k$-$\omega$ model the DDADI scheme converges roughly the same for both the turbulence kinetic energy and the specific dissipation rate equations on both grids. In Figs. 17 and 18 we present the computed surface pressure and skin-friction distributions. The surface pressures predicted with the BL model show the shock location to be much farther downstream than the experiment does. Clearly, there is much better agreement with the data when applying the SA model and $k$-$\omega$ models. According to Wilcox [12], the $k$-$\omega$ model with the stress limiter gives essentially the same results for these types of flows as the shear-stress transport (SST) model of Menter [14] does. This can be verified for Case 10 by comparing the present result with that calculated by Menter and Rumsey [27] using the SST model. As expected the principal difference in the surface skin-friction values computed with the three turbulence models is due to the prediction of the shock location. Even though there is a relatively small difference

14

Table 4: Computational performance for Case 9 using different turbulence models. LSGS(2) used in solving flow equations and DDADI used to solve turbulence equations.

| Model | Grid | CPU Time (sec.) | MG Cycles | Convergence Rate |
|-------|------|-----------------|-----------|------------------|
| BL | $320 \times 64$ | 90 | 91 | 0.720 |
| SA | $320 \times 64$ | 109 | 87 | 0.708 |
| $k$-$\omega$ | $320 \times 64$ | 142 | 92 | 0.722 |
| BL | $640 \times 128$ | 343 | 81 | 0.690 |
| SA | $640 \times 128$ | 504 | 80 | 0.688 |
| $k$-$\omega$ | $640 \times 128$ | 685 | 89 | 0.714 |

Table 5: Computational performance for Case 10 using different turbulence models. LSGS(2) used in solving flow equations and DDADI used to solve turbulence equations.

| Model | Grid | CPU Time (sec.) | MG Cycles | Convergence Rate |
|-------|------|-----------------|-----------|------------------|
| BL | $320 \times 64$ | 105 | 105 | 0.752 |
| SA | $320 \times 64$ | 126 | 99 | 0.739 |
| $k$-$\omega$ | $320 \times 64$ | 178 | 115 | 0.770 |
| BL | $640 \times 128$ | 399 | 95 | 0.729 |
| SA | $640 \times 128$ | 587 | 93 | 0.724 |
| $k$-$\omega$ | $640 \times 128$ | 888 | 116 | 0.772 |

in the shock position obtained with the SA and $k$-$\omega$ models, the behavior of the flow with the two models is different downstream of the shock. The SA model indicates either flow separation or near separation extending to the airfoil trailing edge, but the $k$-$\omega$ model indicates separated flow only from $x/c = 0.55$ to $x/c = 0.70$. Moreover, the attached flow solution with the $k$-$\omega$ model appears to be in better agreement with the experiment. In Table 3 the computed lift and drag coefficients using the different models are given.

The stress limiter of the $k$-$\omega$ model has a significant effect on not only the representation of the physics for this strong transonic case but also the convergence of both the flow and turbulence equations. Figure 19 shows the influence of the stress limiter parameter $C_{lim}$ on convergence. The $C_{lim}$ is varied between 0.0 and 0.95, which is the value used in the previous results. For this range of $C_{lim}$ the number of cycles required to reduce the residual of the flow equations 13 orders increases by $35\%$. The residuals of the turbulence equations are two orders higher when $C_{lim} = 0.95$. It may be possible to improve the convergence through the use of a smoother switching from the unlimited specific dissipation rate to the limited one (see Eq. 20). Figure 20 displays the strong effect on the shock location with the variation of the parameter $C_{lim}$.

## 4.3   Effect of Strain Rate

In all of the previous results we have used the magnitude of the vorticity in defining the turbulence production ($P_k$) terms and the stress limiter of the specific dissipation rate in the $k$-$\omega$ model (see Eqs. 18, 19, and 20). Since Wilcox [10] uses the strain rate $S_{ij}$ to determine $P_k$ rather than the vorticity magnitude in his version of the $k$-$\omega$ model, the question arises as to the effect of this on not only the results but also the convergence of the RK/implicit scheme. To address this question we computed the solution of Case 10 with the strain rate. Figures 21 and 22 show the effect of the two different ways of computing the $P_k$ terms. In Figs. 21(a) and 21(b) we see that there is little difference in the convergence histories for the flow and turbulence equations when using strain rate.

Table 6: Comparison of computed lift and drag coefficients for Case 9 on $640 \times 128$ grid using FMG. For the reference result with SA and $k$-$\omega$ models the residual was reduced 13 orders of magnitude.

| Model | MG Cycles | $C_L$ | $C_D$ |
|-------|-----------|-------|-------|
| SA | 63 | 0.8220 | 0.01662 |
| SA | 10 | 0.8220 | 0.01662 |
| SA | 5 | 0.8213 | 0.01660 |
| | | | |
| $k$-$\omega$ | 69 | 0.8178 | 0.01644 |
| $k$-$\omega$ | 10 | 0.8179 | 0.01644 |
| $k$-$\omega$ | 5 | 0.8191 | 0.01651 |

The comparisons of the surface pressure and skin-friction distributions in Fig. 22 reveal generally only slight differences due to the method of calculating the $P_k$ terms. There is a small downstream shift in the indicated transition location when using strain rate. Although not shown, the solutions obtained for Cases 1 and 9 also show little variation due to the two methods for calculating $P_k$. We should point out that the $C_{lim}$ in the stress limiter of the Wilcox model is 0.875. With the present implementation of the $k$-$\omega$ model, we found that this value resulted in the computed shock location being downstream of the measured data. By using $C_{lim} = 0.96$, nearly the same value used when computing $P_k$ with vorticity magnitude, we obtained good agreement with the data. There are other differences between the current implementation of the model and the 2006 Wilcox implementation that may possibly explain the different value for the parameter $C_{lim}$ (see Section 2.2).

## 4.4   Effect of Full Multigrid

Convergence of the solution, to the approximate level of the truncation error, can be accelerated by implementing full multigrid (FMG). We now consider the performance of the RK/implicit scheme with FMG when applying the SA and $k$-$\omega$ models. The residual and lift coefficient ($C_L$) convergence histories for the 3-stage RK/implicit scheme when applying the SA model and using FMG are shown in Fig. 23. The calculation was done for Case 9 with the $640 \times 128$ grid using 3 levels of refinement, which contain 3, 4, and 5 grids. On each level multigrid was executed until either 100 cycles were completed or the residual was reduced 13 orders of magnitude. The CFL number for the flow equations was increased to 1000 over the first 10 cycles of the first refinement level and maintained on all the remaining levels. As seen in Table 6, with only 5 cycles on the final level the $C_L$ error relative to the converged value is less than 0.1%. Agreement with the converged $C_L$ and $C_D$ is obtained to 4 significant figures in 10 cycles. As evident in Fig. 24 the surface pressure and skin-friction distributions at 5 cycles is nearly identical to the corresponding one with the residual reduced 13 orders of magnitude. In Figs. 25 and 26 we present the convergence histories and solution comparisons when applying the $k$-$\omega$ model. After 5 cycles both the $C_L$ and $C_D$ are within 0.5% of the converged value. Here again to plotting accuracy we see essentially the same surface pressure and skin-friction distributions for the 5 cycle and converged solutions.

## 5   Concluding Remarks

In this work we have investigated the performance of the RK/implicit algorithm for solving the RANS equations when different types of turbulence models are applied. Airfoil flows have been solved with three turbulence models: (1) the algebraic model of Baldwin and Lomax, (2) the one-equation model of Spalart and Allmaras, (3) the two-equation ($k$-$\omega$) model of Wilcox. The fluid dynamic and turbulence equations have been solved in a loosely coupled manner. This approach has allowed examination of the convergence properties of each set of equations. The fluid dynamic equations have been solved with the RK/implicit scheme and multigrid. Both point and line solves have been considered to approximate the inverse of the implicit operator. Line solves are in general necessary to appropriately treat the stronger coupling of the flow equations in an airfoil wake when the

eddy viscosity field is determined with either the SA or $k$-$\omega$ models. The equation set for each turbulence model has been solved only on the solution grid with a DDADI scheme. For both the fluid dynamic and turbulence equations a CFL of 1000 has been used.

To evaluate each part of the numerical algorithm for solving the loosely coupled system of equations, we have used three of the standard RAE airfoil test cases (Cases 1, 9, and 10). For all cases computational results have been obtained on a standard grid ($320 \times 64$ cells) and on a fine grid ($640 \times 128$ cells) in order to indicate the effect of mesh refinement on convergence. We have investigated not only the convergence behavior of the algorithm but also the effects of the turbulence modeling on the solutions. In all cases the flow equations converged as fast, if not faster, when using the SA and $k$-$\omega$ models instead of the BL model. Furthermore, these equations converged at similar rates on both the standard and fine grids. For the equation sets of the SA and $k$-$\omega$ models, we have shown that the residuals can be reduced about 10 orders of magnitude when the residuals for the flow equations are reduced 13 orders. With the DDADI scheme we have not observed a strong effect on the rate of convergence due to mesh refinement.

With all turbulence models reasonable agreement has been obtained with the experimental surface pressure and skin-friction distributions for Cases 1 and 9. For Case 10, where there is a sufficiently strong shock to induce significant separation, only the SA and $k$-$\omega$ models exhibit good agreement with the measured data. The $k$-$\omega$ model requires the introduction of a stress limiter for the specific dissipation rate. With the stress limiter the $k$-$\omega$ model can produce essentially the same results obtained with Menter's SST model. Without this limiter the shock location is predicted too far downstream.

In applying the RK/implicit scheme with j-line SGS a convergence rate of approximately 0.7 has been obtained for both Case 1 and Case 9 on the standard and fine grids with all turbulence models. The convergence rates of the DDADI scheme on each grid are similar for a given turbulence model. For Case 10 the flow solver has converged at rates of about 0.74 and 0.73 with the BL and SA models, respectively. With the $k$-$\omega$ models there is some deterioration in the average convergence rate of the scheme ($\approx 0.77$). Yet, the asymptotic rate is about the same as obtained with the other models. When solving the PDEs of the SA and $k$-$\omega$ models the DDADI scheme converges roughly at the same rate as for Case 9. As part of the convergence investigation we have also considered the effect of FMG. With only 5 multigrid cycles on the finest grid we have essentially obtained the solution to plotting accuracy for Case 9 with both the SA and $k$-$\omega$ models.

At this point we have demonstrated that the 2-D RANS equations and transport-type equations can be solved efficiently in a loosely coupled manner. In the continuation of this work we plan to consider several enhancements of the current algorithm to improve efficiency and robustness. The DDADI scheme with subiteration was chosen in this initial effort to solve the PDE equation set of a turbulence model because it is an effective solver, and it allowed a reference efficiency to be established. With any scheme for solving the equation set of a turbulence model there will be slowdown in convergence on sufficiently fine meshes. To reduce any convergence effects due to mesh density we will include multigrid in the scheme for solving the PDEs of the turbulence models. By introducing multigrid the role of what was the solver will be changed to that of a high-frequency smoother. Various smoothers will be considered, including the RK/implicit scheme. An acceptable smoother must be effective in three dimensions. Ultimately, the objective is to develop both loosely coupled and fully coupled algorithms that are reliable and efficient in both two and three dimensions.

So far we have not directly addressed the issue of robustness when solving the turbulence equations. A powerful technique for increasing reliability of the complete algorithm is the Krylov subspace iterative method. Frequently, there are only a few error modes that inhibit or stall the convergence of a scheme. Since the Krylov method works on the dominant error modes, it can effectively annihilate these troublesome error components. The effects of a Krylov method on the performance of the scheme will also be investigated.

# Appendix

In section 4.1 we showed that the rapid increase in the lateral extent of the near wake $\mu_t$ field determined with the $k$-$\omega$ model (see Fig. 5) can be significantly affected by increasing the mesh resolution. Further investigation has indicated that accuracy is a controlling factor for obtaining reasonable physical behavior in the near wake development of the $\mu_t$ field. In this investigation we also determined that inclusion of the cross-diffusion term

17

produced only a small effect on the $\mu_t$ behavior in the initial wake region. Figure 27(a) displays the trailing edge region of the $320 \times 64$ grid used in the previous calculations. For this grid, which was generated by a hyperbolic method, there is a spreading out of the radial lines. By choosing different grid generation parameters we generated a new grid with a dramatically reduced spreading effect, as shown in Fig. 27(b). We designate the original and new grids as the reference and modified $320 \times 64$ grids, respectively. The influence of the modified grid on the $\mu_t$ variation is displayed in Fig. 28. Clearly, there is a significant reduction in the lateral extent of the non-zero $\mu_t$ in the near wake region. Comparing the profiles of Fig. 28 with those of Fig. 6(c) and Fig. 6(d) we see that the $\mu_t$ profiles on a given grid density are actually quite similar, with some differences due to lateral extent.

Another factor that can effect the near wake behavior is the order of approximation of the convection terms in the model. White [28] has computed solutions for Case 1 with both a first-order and a second-order upwind approximation of the convection terms in essentially the 2006 Wilcox $k$-$\omega$ model [10]. He solved the fully coupled RANS and turbulence model equations with a second-order, finite-volume algorithm [29]. On the present reference $640 \times 128$ grid White obtained very similar $\mu_t$ contours to those of Fig. 5(d) with the first-order approximation of the convection terms. Using a second-order upwind approximation he obtained similar $\mu_t$ contours to those of Fig. 28(c). These results suggests that the convection terms play a much more important role in a free-shear flow with the $k$-$\omega$ model than the SA model. Consequently, the $k$-$\omega$ model is much more sensitive to the accuracy of the convection terms in the wake flow than the SA model.

# References

[1] E. Dick, A flux-vector splitting method for steady Navier-Stokes equations, *Int. J. Numer. Meth. Fluids* 8 (1988) 317–326.

[2] J. Wackers and B. Koren, Multigrid solution method for the steady RANS equations. *J. Comput. Phys.* 226 (2007) 1784–1807.

[3] C.-C. Rossow, Efficient computation of compressible and incompressible flows. *J. Comput. Phys.* 220 (2007) 879–899.

[4] R. C. Swanson, E. Turkel, and C.-C. Rossow, Convergence acceleration of Runge-Kutta Schemes for solving the Navier-Stokes equations, *J. Comput. Phys.* 224 (2007) 365–388.

[5] B. S. Baldwin and H. Lomax, Thin layer approximation and algebraic model for separated flows, *AIAA Paper* 78-257, 1978.

[6] R. C. Swanson and E. Turkel, Multistage schemes with multigrid for Euler and Navier-Stokes equations, NASA TP 3631, 1997.

[7] P. R. Spalart and S. R. Allmaras, A one-equation turbulence model for aerodynamic flows, *La Recherche Aerospatiale* 1 (1994) 5–21.

[8] S. L. Krist, R. T. Biedron, and C. L. Rumsey, CFL3D user's manual, NASA TM 1998-208444, June 1998.

[9] C. L. Rumsey, Apparent transition behavior of widely-used turbulence models, *AIAA Paper* 2006-3906, June 2006.

[10] D. C. Wilcox, Turbulence Modeling for CFD, DCW Industries, Inc., 2006.

[11] D. C. Wilcox, Reassessment of the scale-determining equation for advanced turbulence models, *AIAA J.* 26 (1988) 1299–1310.

[12] D. C. Wilcox, Formulation of the $k$-$\omega$ turbulence model revisited, *AIAA Paper* 2007-1408, January 2007.

[13] P. G. Huang, Physics and computations of flows with adverse pressure gradients, *Modeling Complex Turbulent Flows*, M. Salas et al. editors, Kluwer, 1999, 245–258.

[14] F. R. Menter, Zonal two equation $k$-$\omega$ turbulence model for aerodynamic flows, *AIAA Paper* 93-2906, July 1993.

[15] P. L. Roe, Approximate Riemann solvers, parameter vectors and difference schemes, *J. Comput. Phys.*, 43, 357–372, 1981.

[16] A. Jameson, The evolution of computational methods in aerodynamics, *J. Appl. Mech.*, 50 (4b), 1052–1070, 1983.

[17] C.-C. Rossow, Convergence acceleration for solving the compressible Navier-Stokes equations, *AIAA J.*, 44, 345-352, 2006.

[18] D. J. Mavriplis, Multigrid strategies for viscous flow solvers on anisotropic unstructured meshes, *J. Comput. Phys.*, 145, 141–165, 1998.

[19] B. Van Leer, C.-H. Tai, and K. G. Powell, Design of optimally smoothing multi-stage schemes for the Euler equations, *AIAA Paper* 89-1933, 1989.

[20] G. H. Klopfer, R. F. Van der Wijngaart, C. M. Hung, J. T. Onufer, A diagonalized diagonal dominant alternating direction implicit (D3ADI) scheme and subiteration correction, *AIAA Paper* 98-2824, June 1998.

[21] R. W. MacCormack and T. H. Pulliam, Assessment of a new numerical procedure for fluid dynamics, *AIAA Paper* 98-2821, June 1998.

[22] J. Bardina and C. K. Lombard, Three dimensional hypersonic flow simulations with the CSCM implicit upwind Navier-Stokes Method, *AIAA Paper* 87-1114, June 1987.

[23] V. Venkatakrishnan, Improved convergence of compresible Navier-Stokes solvers, *AIAA Paper* 98-2967, June 1998.

[24] P. C. Walsh and T. Pulliam, The effect of turbulence model solution on viscous flow problems, *AIAA Paper* 2001-1018,

[25] P. H. Cook, M. A. McDonald, M. C. P. Firmin, Aerofoil RAE 2822 pressure distributions and boundary layer and wake measurements, AGARD-AR-138, 1979.

[26] T. H. Pulliam, R. W. MacCormack, and S. Venkateswaran, Convergence characteristics of approximate factorization methods, Lecture Notes in Physics, 16th International Conference on Numerical Methods in Fluid Dynamics, Arcachon, France, July 6–10, 1998.

[27] F. R. Menter and C. L. Rumsey, Assessment of two-equation turbulence models for transonic flows, *AIAA Paper* 94-2343, June 1994.

[28] J. A. White, private communication, 2008.

[29] J. A. White and J. H. Morrison, A pseudo-temporal multi-grid relaxation scheme for solving the parabolized Navier-Stokes equations, *AIAA Paper* 99-3360, 1999.
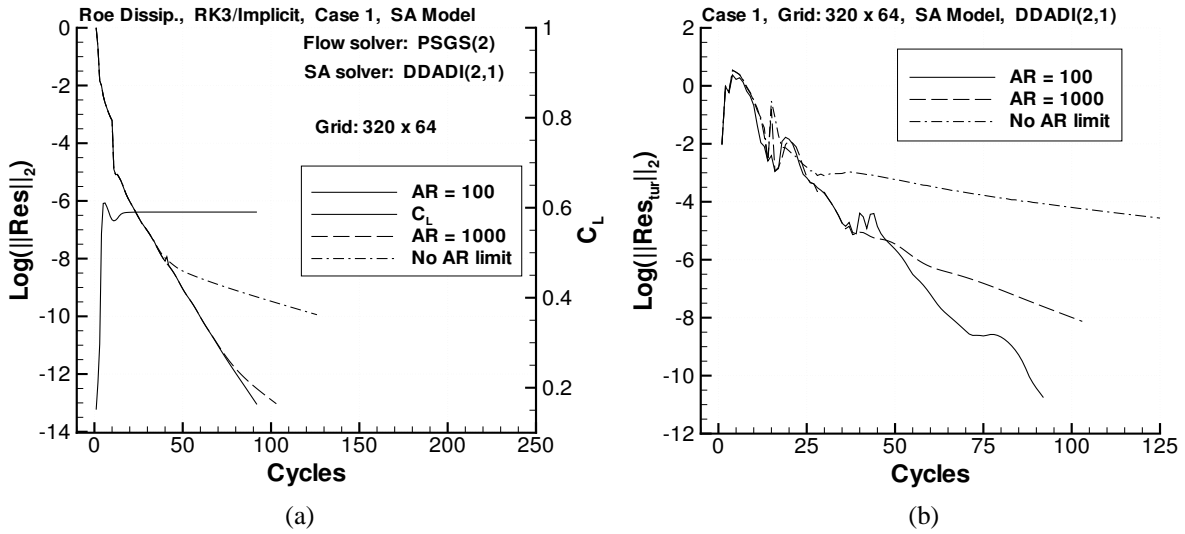
Figure 3: Effect of wake aspect ratio on convergence of Case 1 with SA model on $320 \times 64$ grid. (a) Flow equations, (b) SA equation.
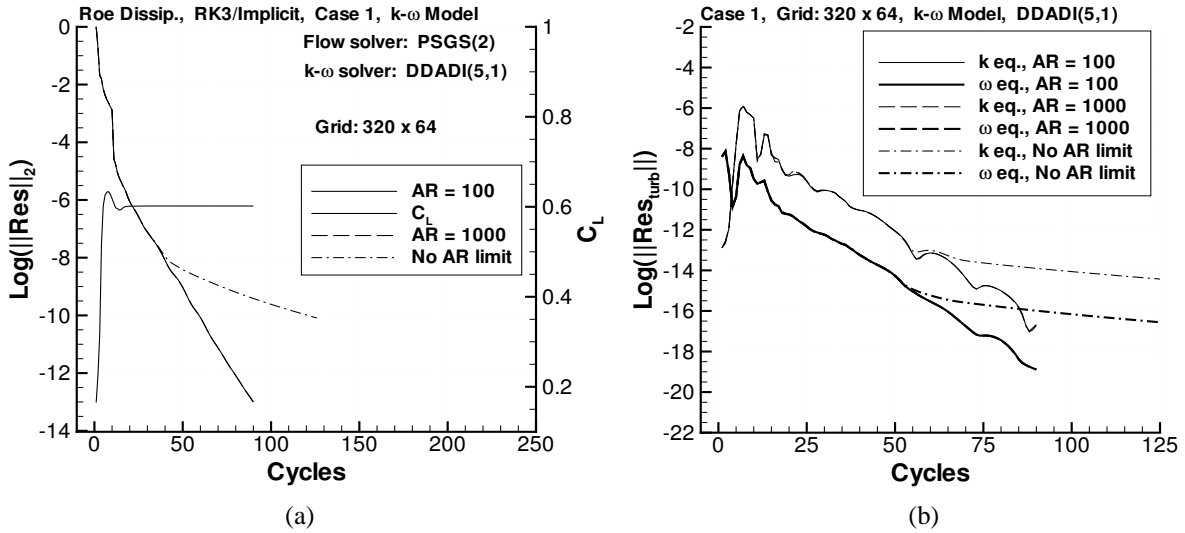


Figure 4: Effect of wake aspect ratio on convergence of Case 1 with $k$-$\omega$ model on $320 \times 64$ grid. (a) Flow equations, (b) $k$-$\omega$ equations.
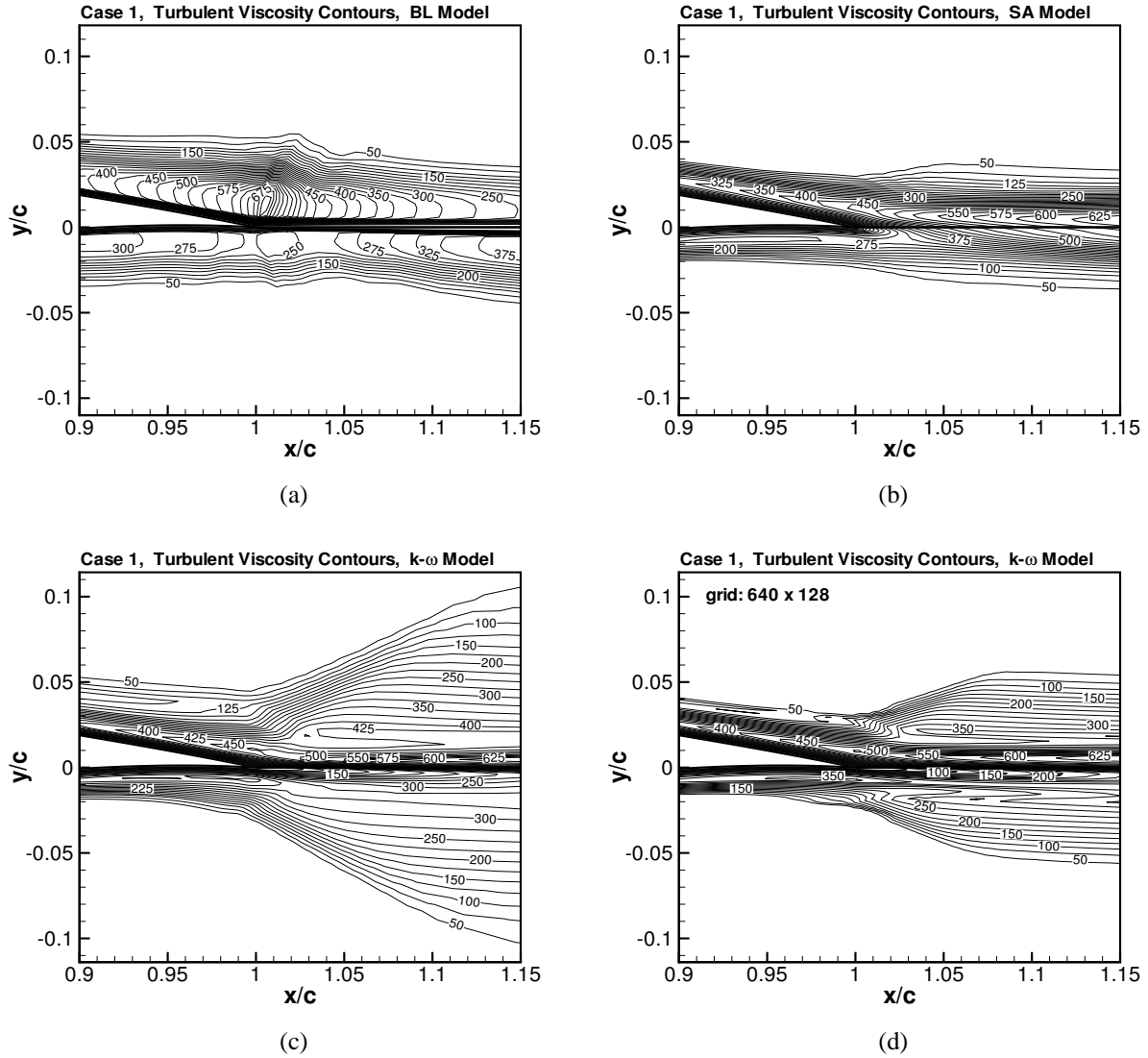
Figure 5: Contours of turbulent viscosity near trailing edge for Case 1, computed with BL, SA, and $k$-$\omega$ models. On $320 \times 64$ grid: (a) BL model, (b) SA model, (c) $k$-$\omega$ model. Effect of grid refinement: (d) $k$-$\omega$ model, $640 \times 128$ grid.

22
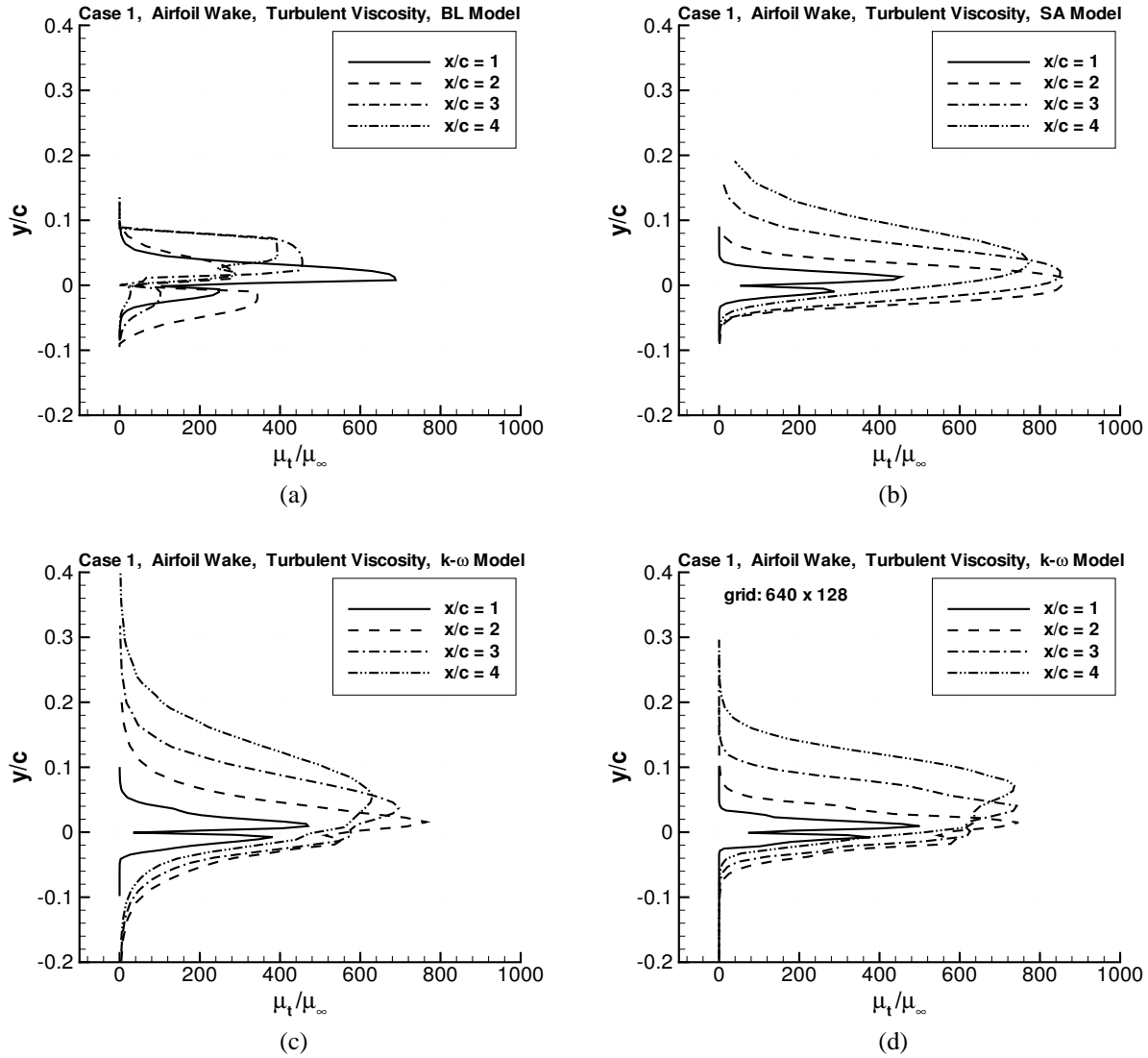
Figure 6: Turbulent viscosity profiles in the airfoil wake for Case 1, computed with BL, SA, and $k$-$\omega$ models. On $320 \times 64$ grid: (a) BL model, (b) SA model, (c) $k$-$\omega$ model. Effect of grid refinement: (d) $k$-$\omega$ model, $640 \times 128$ grid.
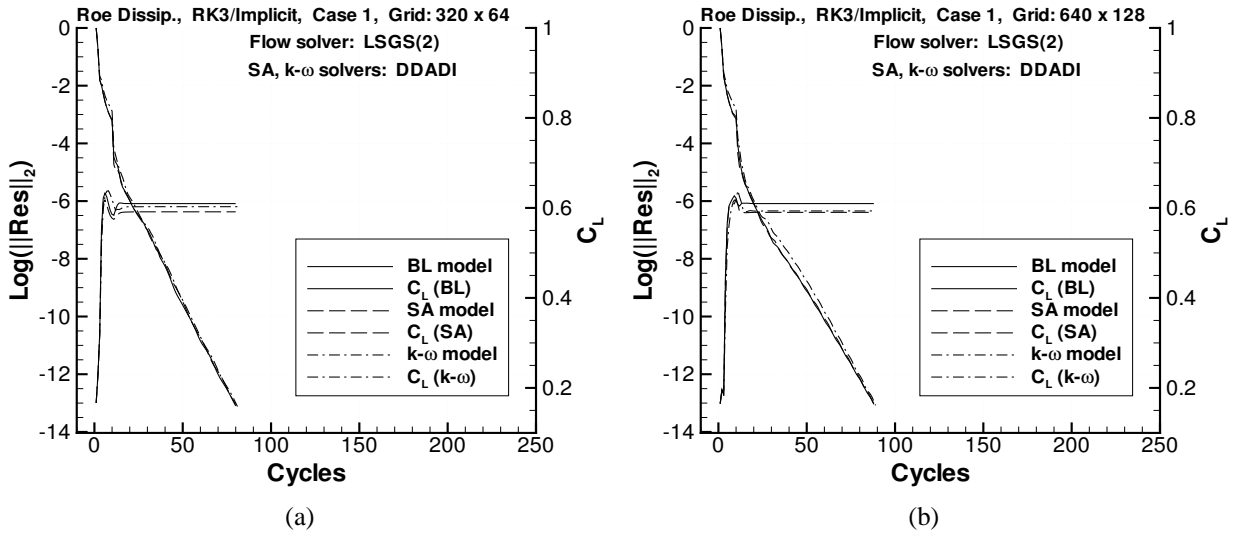
Figure 7: Convergence histories for Case 1 on two grids with BL, SA, and $k$-$\omega$ models. Flow equations solved with line SGS(2) and transport-type equations solved with DDADI. (a) $320 \times 64$ grid, (b) $640 \times 128$ grid.
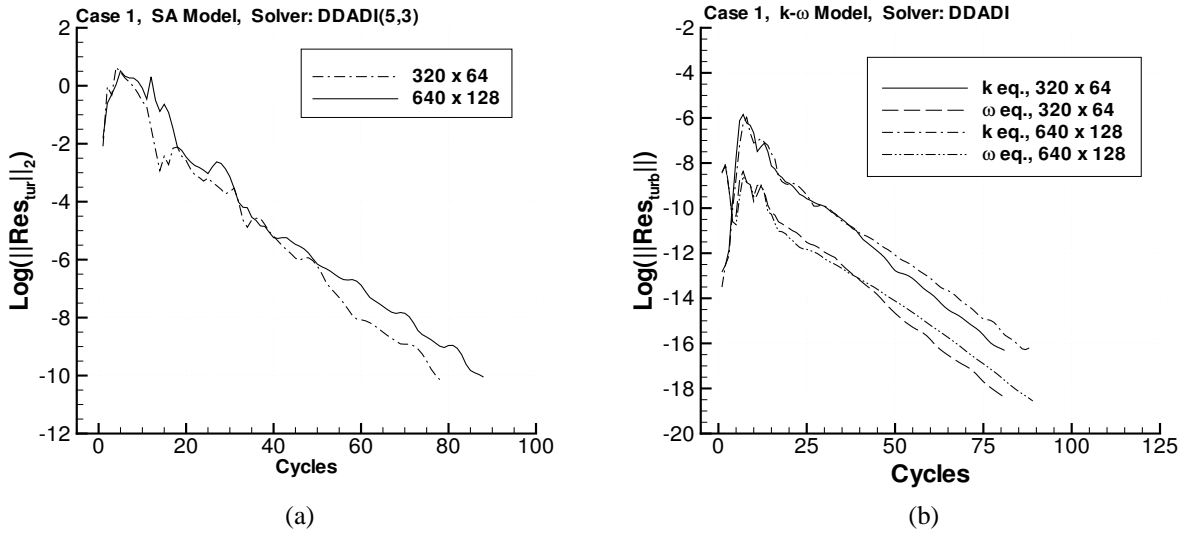


Figure 8: Convergence histories of SA and $k$-$\omega$ models for Case 1 on two grids. Transport-type equations solved with DDADI. (a) SA model, (b) $k$-$\omega$ model.
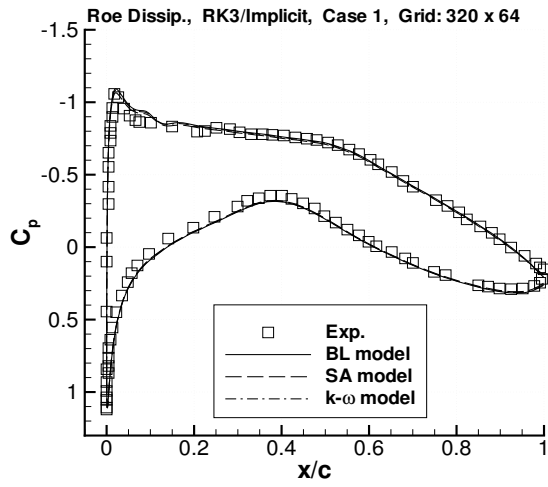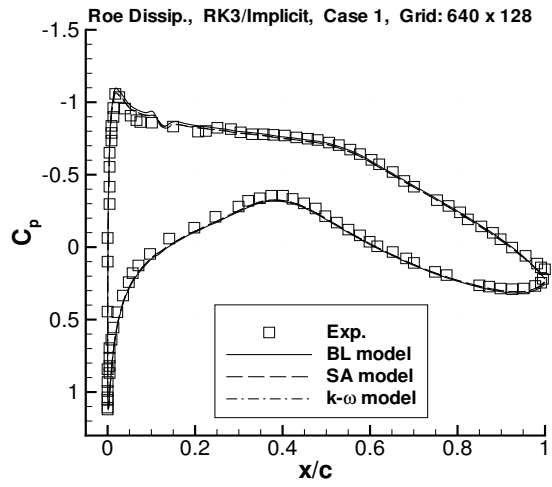
Figure 9: Surface pressure distributions for Case 1 on two grids with BL, SA, and $k$-$\omega$ models. (a) $320 \times 64$ grid, (b) $640 \times 128$ grid.
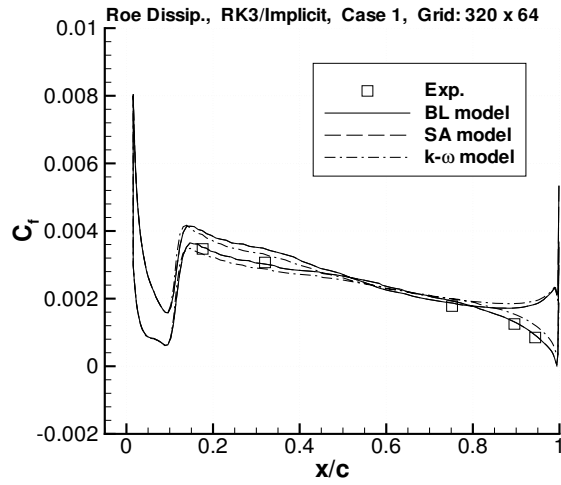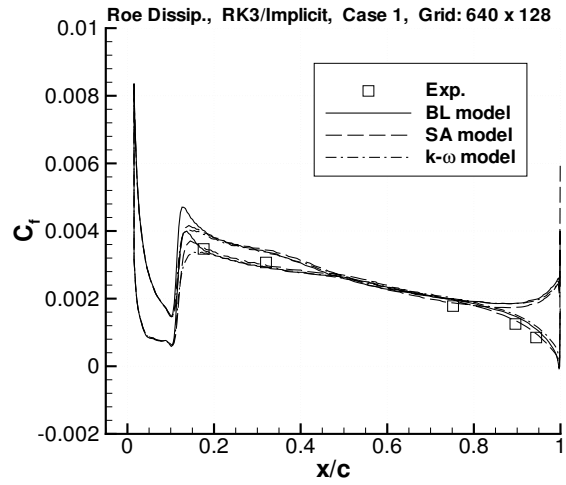


Figure 10: Surface skin-friction distributions for Case 1 on two grids with BL, SA, and $k$-$\omega$ models. (a) $320 \times 64$ grid, (b) $640 \times 128$ grid.
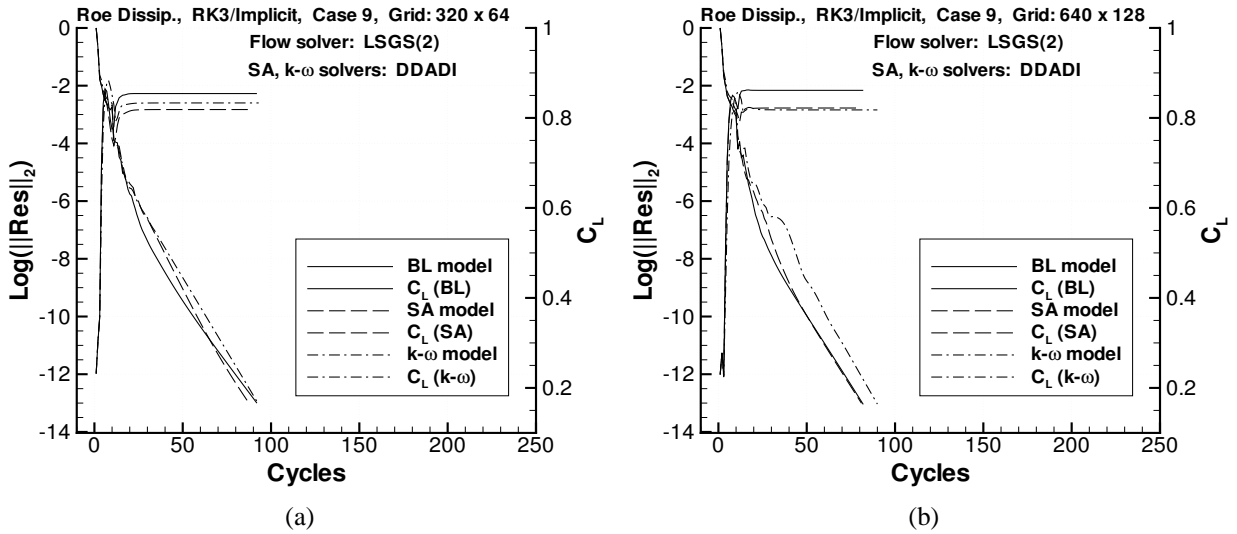
Figure 11: Convergence histories for Case 9 on two grids with BL, SA, and $k$-$\omega$ models. Flow equations solved with line SGS(2) and transport-type equations solved with DDADI. (a) $320 \times 64$ grid, (b) $640 \times 128$ grid.
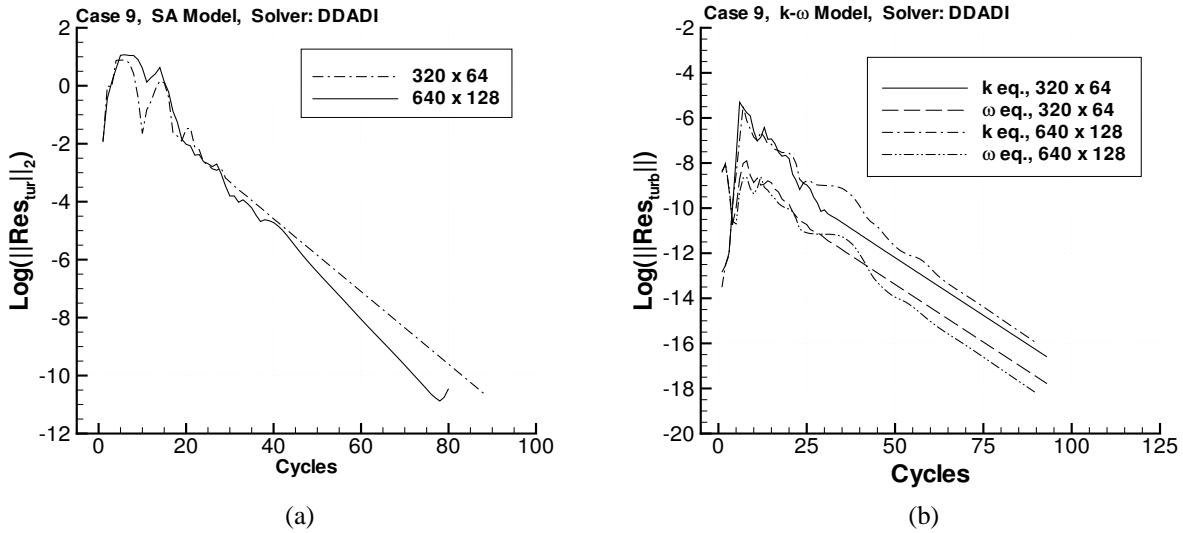


Figure 12: Convergence histories of SA and $k$-$\omega$ models for Case 9 on two grids. Transport-type equations solved with DDADI. (a) SA model, (b) $k$-$\omega$ model.

26
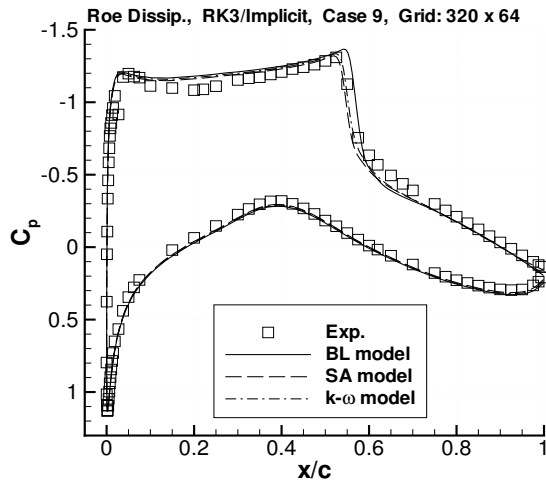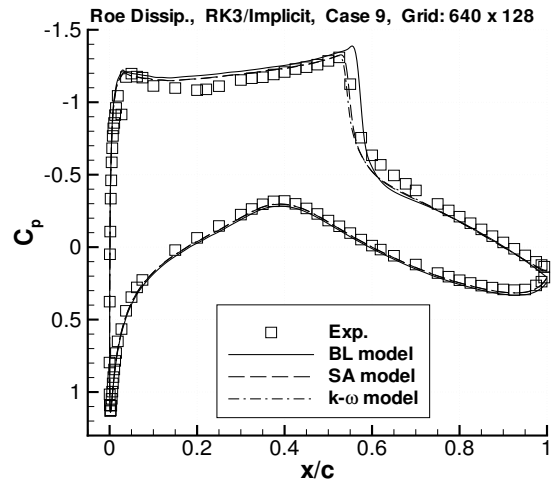
Figure 13: Surface pressure distributions for Case 9 on two grids with BL, SA, and $k$-$\omega$ models. (a) $320 \times 64$ grid, (b) $640 \times 128$ grid.
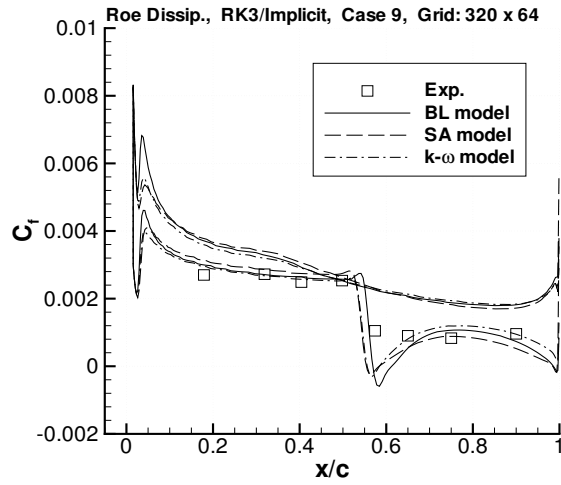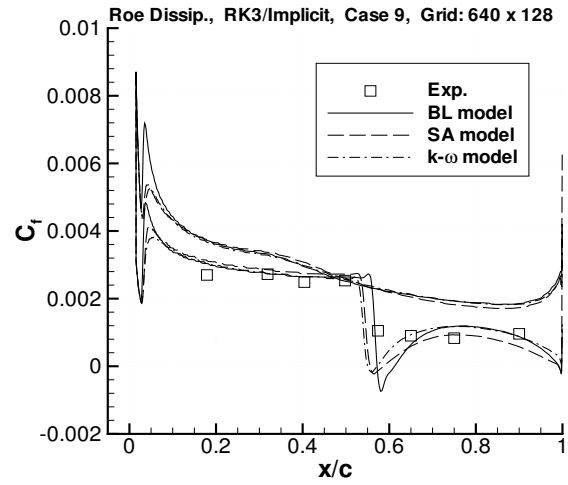


Figure 14: Surface skin-friction distributions for Case 9 on two grids with BL, SA, and $k$-$\omega$ models. (a) $320 \times 64$ grid, (b) $640 \times 128$ grid.
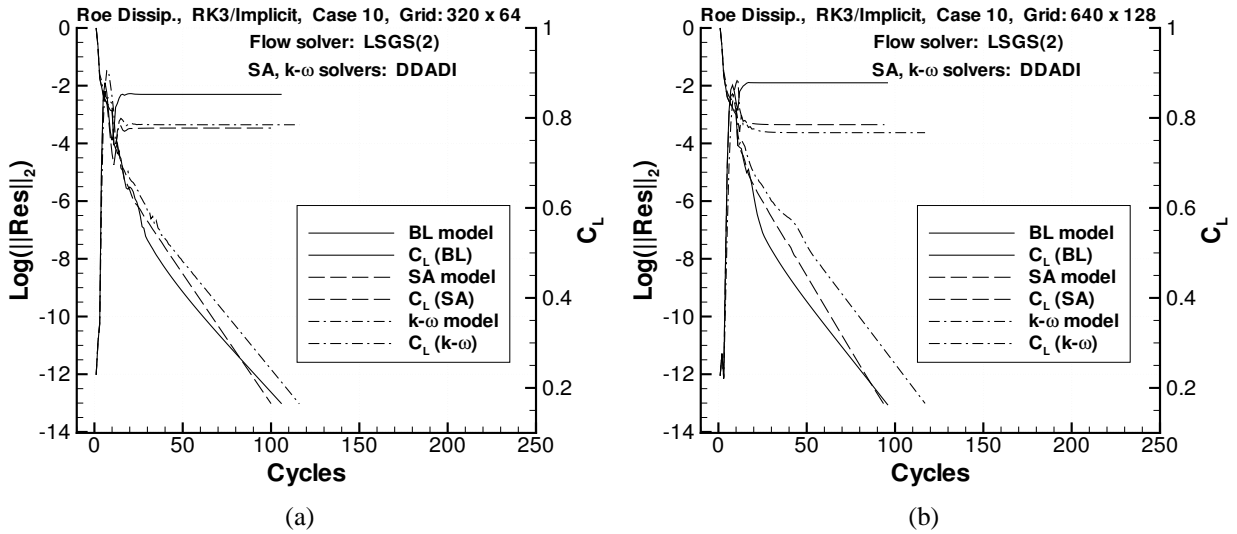
Figure 15: Convergence histories for Case 10 on two grids with BL, SA, and $k$-$\omega$ models. Flow equations solved with line SGS(2) and transport-type equations solved with DDADI. (a) $320 \times 64$ grid, (b) $640 \times 128$ grid.
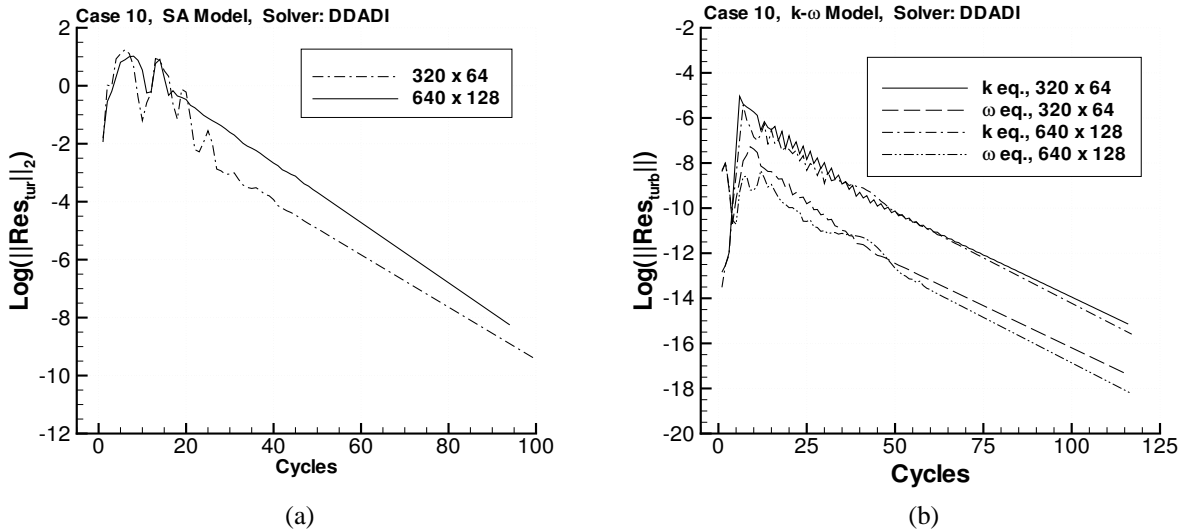


Figure 16: Convergence histories of SA and $k$-$\omega$ models for Case 10 on two grids. Transport-type equations solved with DDADI. (a) SA model, (b) $k$-$\omega$ model.
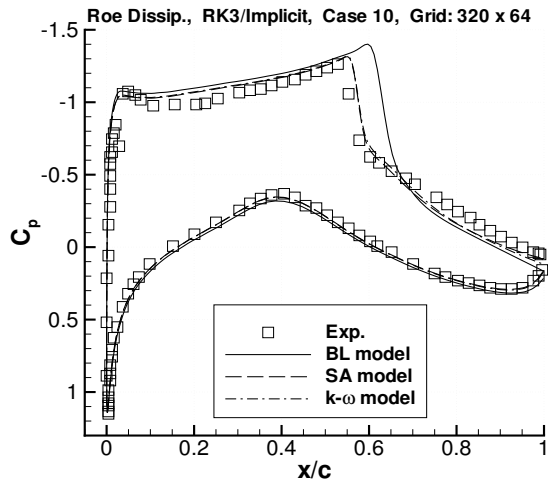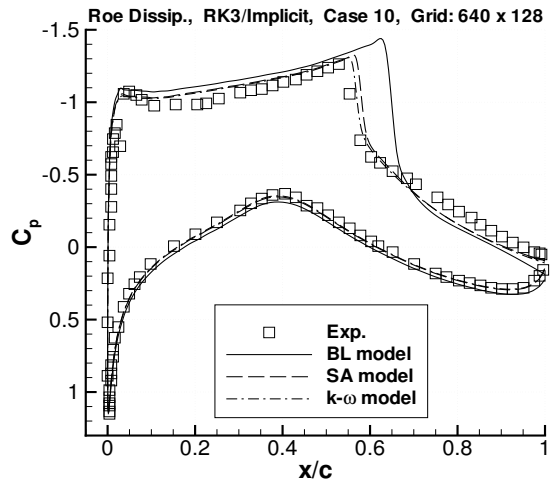
Figure 17: Surface pressure distributions for Case 10 on two grids with BL, SA, and $k$-$\omega$ models. (a) $320 \times 64$ grid, (b) $640 \times 128$ grid.
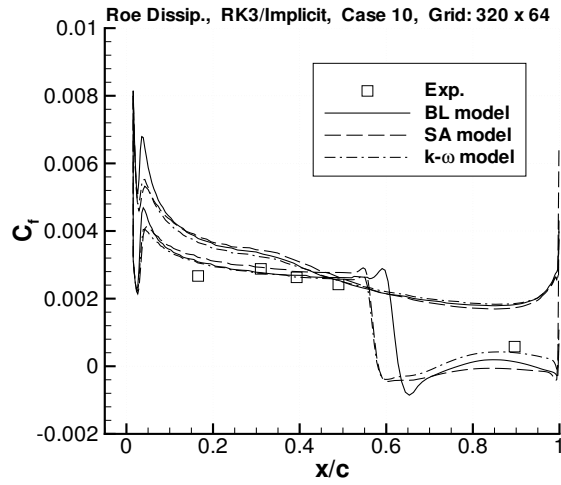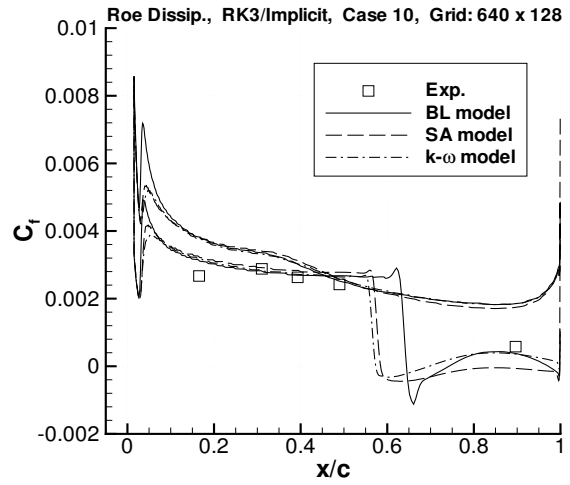


Figure 18: Surface skin-friction distributions for Case 10 on two grids with BL, SA, and $k$-$\omega$ models. (a) $320 \times 64$ grid, (b) $640 \times 128$ grid.

29
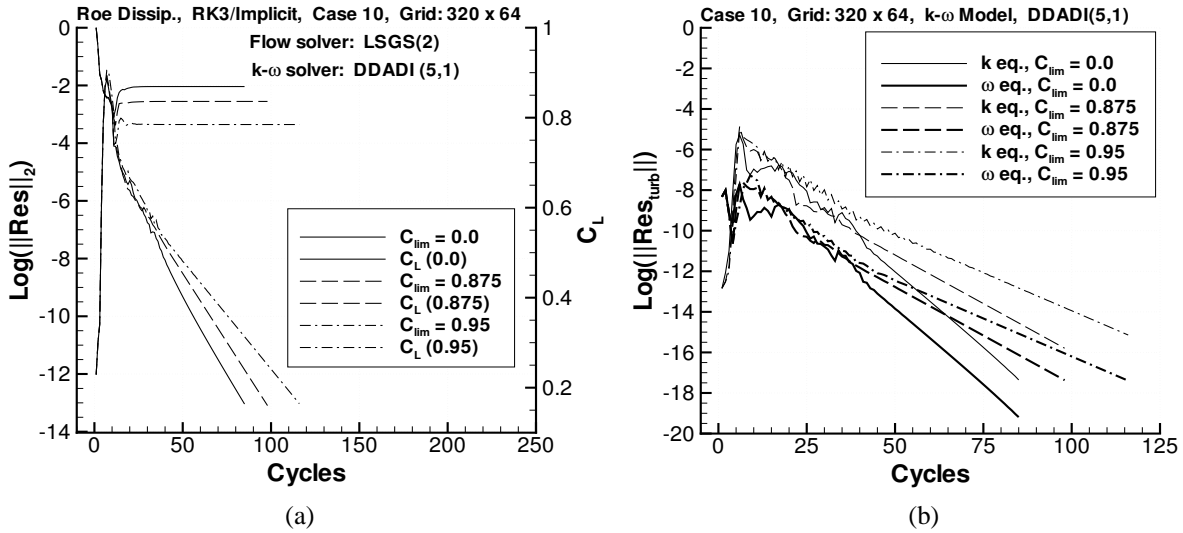
Figure 19: Effect of stress limiter of $k$-$\omega$ model on convergence histories of fluid and turbulence equations (Case 10, $320 \times 64$ grid). Flow equations solved with line SGS(2) and $k$-$\omega$ model equations solved with DDADI(5,1). (a) Flow equations, (b) turbulence equations.
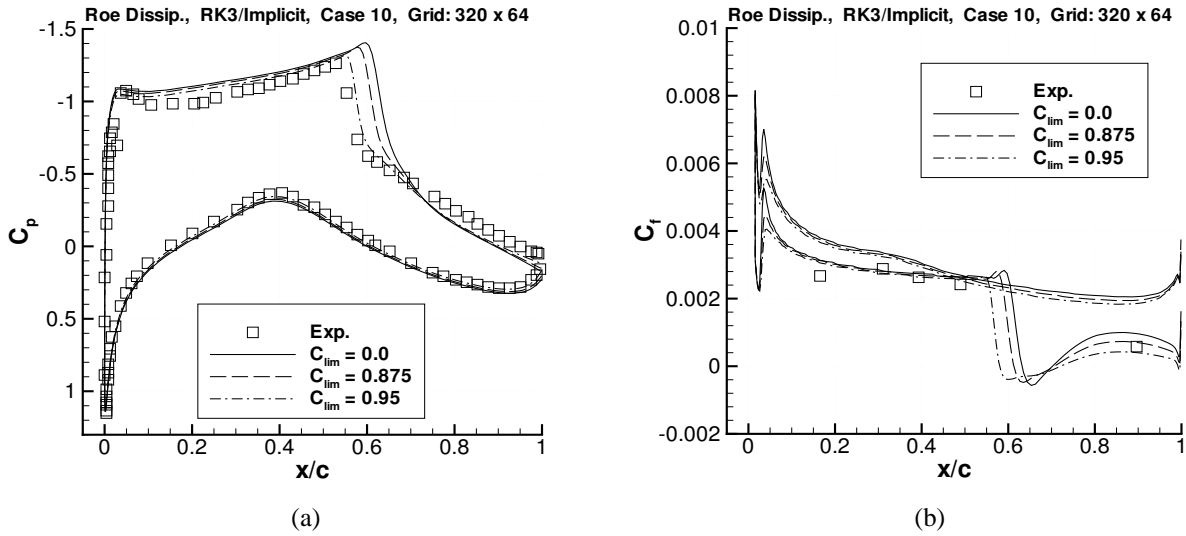


Figure 20: Effect of stress limiter of $k$-$\omega$ model on surface pressure and skin-friction distributions for Case 10 ($320 \times 64$ grid). (a) Surface pressures, (b) Surface skin-friction.

30
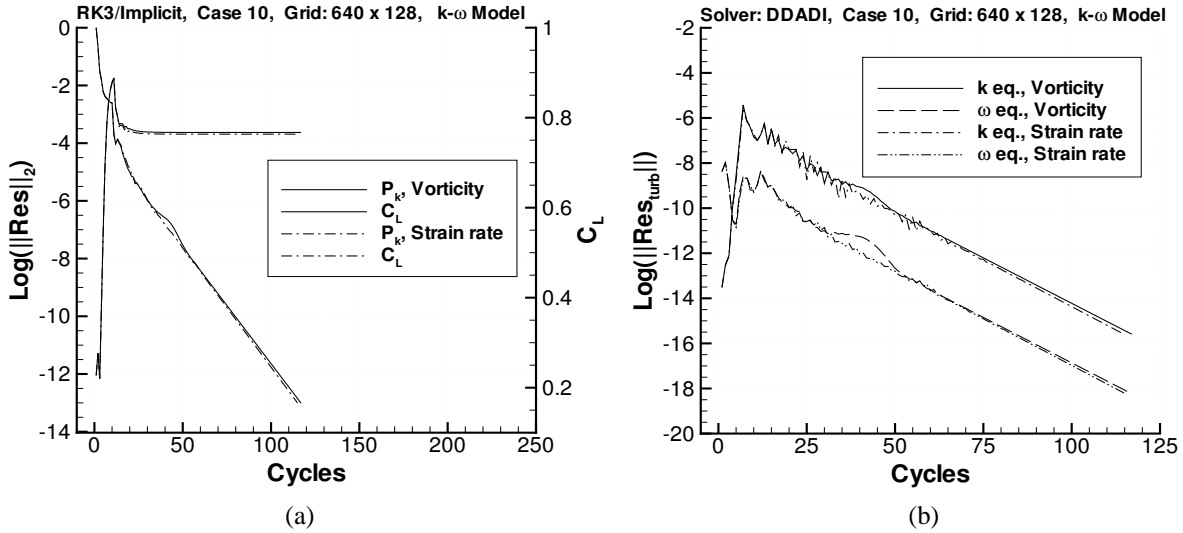
Figure 21: Effect of computing turbulence production ($P_k$) terms of $k$-$\omega$ model with vorticity or strain rate. Convergence histories of fluid and turbulence equations (Case 10, $640 \times 128$ grid). Flow equations solved with j-line SGS(2) and $k$-$\omega$ model equations solved with DDADI(5,1). (a) Flow equations, (b) turbulence equations.
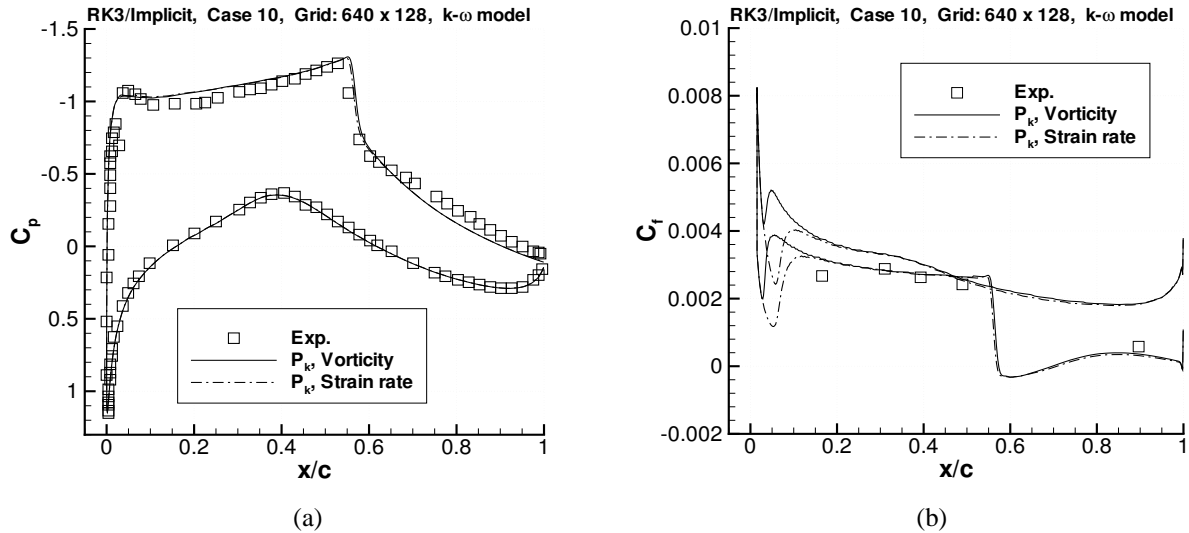


Figure 22: Effect of two ways of computing $P_k$ terms of $k$-$\omega$ model on surface pressure and skin-friction distributions for Case 10 ($320 \times 64$ grid). (a) Surface pressures, (b) Surface skin-friction.
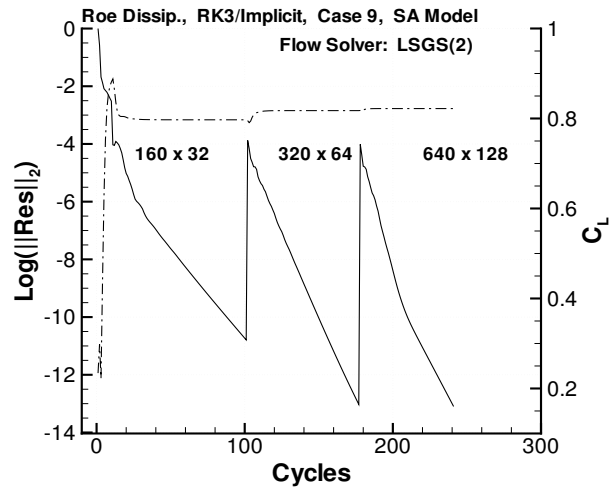
Figure 23: Convergence history of flow equations with FMG (3 levels of refinement) for Case 9. Flow equations solved with j-line SGS(2) and SA model equation solved with DDADI.
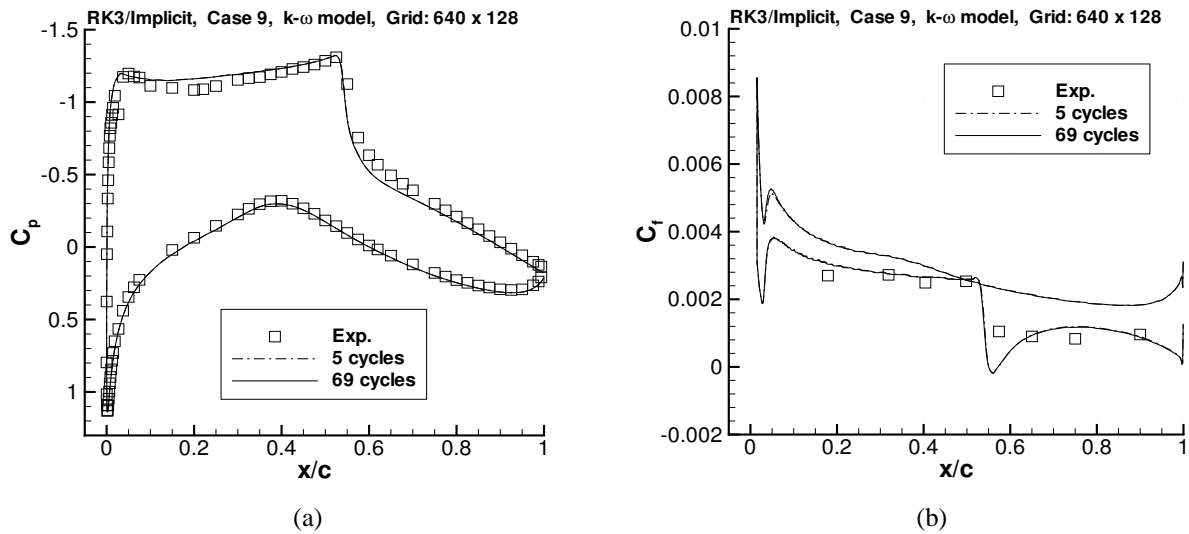


(a)



(b)
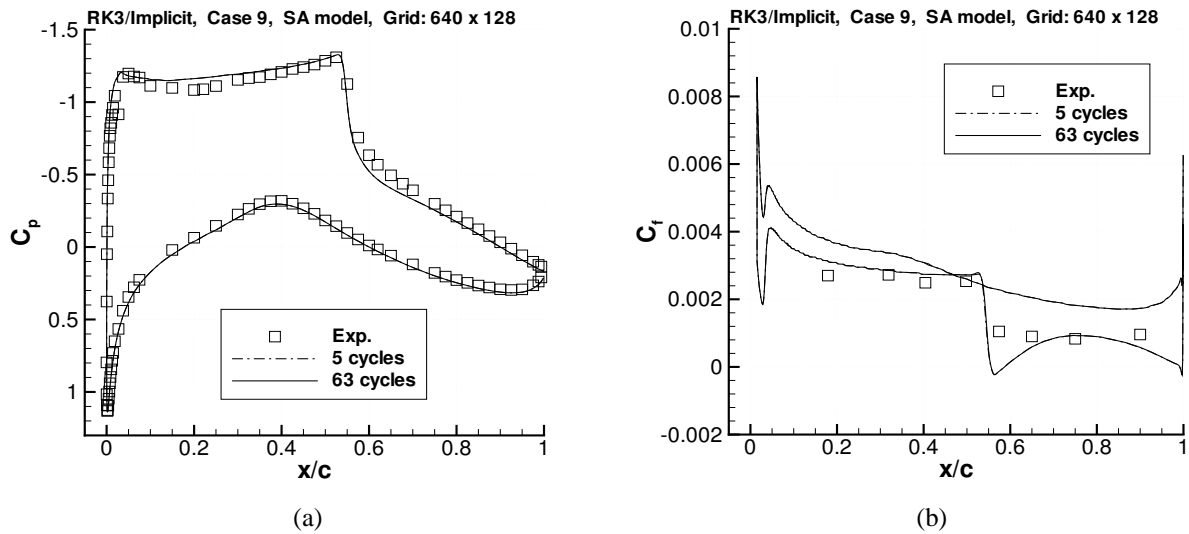
Figure 24: Comparison of surface pressure and skin-friction distributions at 5 cycles and 63 cycles (residual reduced 13 orders) computed for Case 9 with SA model. FMG used to solve flow equations. (a) Surface pressures, (b) Surface skin-friction.
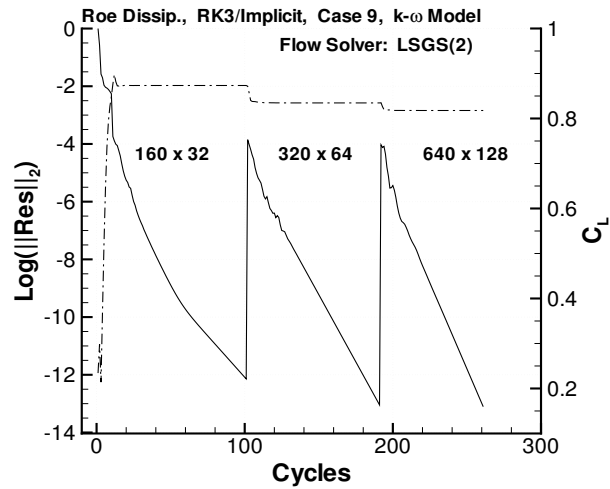
Figure 25: Convergence history of flow equations with FMG (3 levels of refinement) for Case 9. Flow equations solved with j-line SGS(2) and $k$-$\omega$ model equations solved with DDADI.



(a)

(b)

Figure 26: Comparison of surface pressure and skin-friction distributions at 5 cycles and 69 cycles (residual reduced 13 orders) computed for Case 9 with $k$-$\omega$ model. FMG used to solve flow equations. (a) Surface pressures, (b) Surface skin-friction.
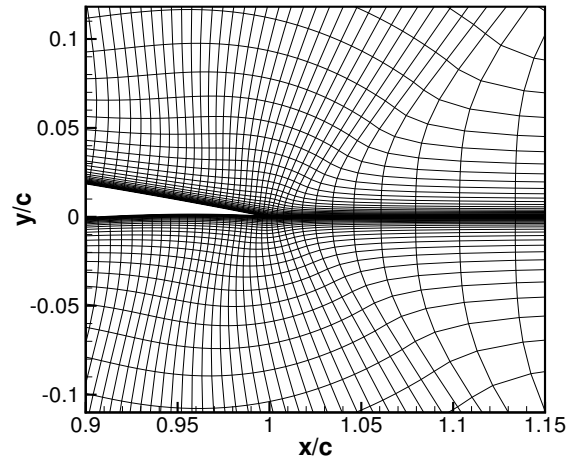
(a) Reference grid.
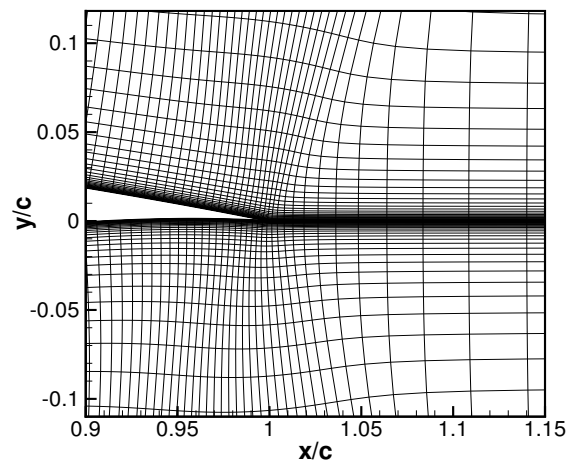


(b) Modified grid.

Figure 27: Airfoil trailing edge region of two different grids with $320 \times 64$ cells.
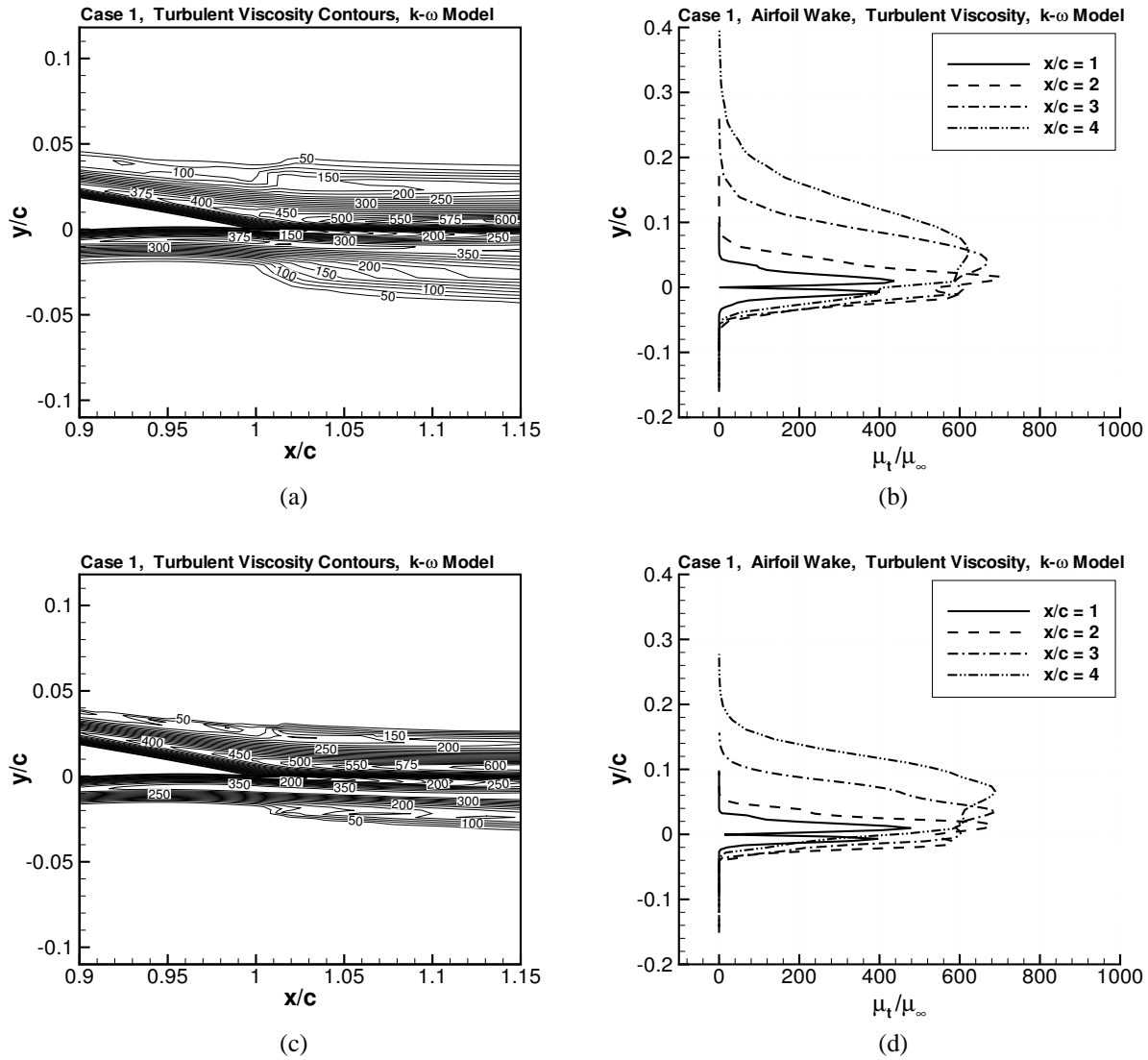
Figure 28: Effect of modified grid on turbulent viscosity contours and profiles near the trailing edge for Case 1, computed with the $k$-$\omega$ model. On $320 \times 64$ grid: (a) contours, (b) profiles. On $640 \times 128$ grid: (c) contours, (d) profiles.

# REPORT DOCUMENTATION PAGE

| 1. REPORT DATE *(DD-MM-YYYY)* | 2. REPORT TYPE | 3. DATES COVERED *(From - To)* |
|---|---|---|
| 01-08-2008 | Technical Memorandum | |

**4. TITLE AND SUBTITLE**

An Initial Investigation of the Effects of Turbulence Models on the Convergence of the RK/Implicit Scheme

**5a. CONTRACT NUMBER**

**5b. GRANT NUMBER**

**5c. PROGRAM ELEMENT NUMBER**

**6. AUTHOR(S)**

R. C. Swanson and C.-C. Rossow

**5d. PROJECT NUMBER**

**5e. TASK NUMBER**

**5f. WORK UNIT NUMBER**

561581.02.08.07.20.02

**7. PERFORMING ORGANIZATION NAME(S) AND ADDRESS(ES)**

NASA Langley Research Center
Hampton, VA 23681-2199

**8. PERFORMING ORGANIZATION REPORT NUMBER**

L–19509

**9. SPONSORING/MONITORING AGENCY NAME(S) AND ADDRESS(ES)**

National Aeronautics and Space Administration
Washington, DC 20546-0001

**10. SPONSOR/MONITOR'S ACRONYM(S)**

NASA

**11. SPONSOR/MONITOR'S REPORT NUMBER(S)**

NASA/TM–2008–215342

**12. DISTRIBUTION/AVAILABILITY STATEMENT**

Unclassified-Unlimited
Subject Category 64
Availability: NASA CASI (301) 621-0390

**13. SUPPLEMENTARY NOTES**

An electronic version can be found at http://ntrs.nasa.gov.

**14. ABSTRACT**

A three-stage Runge-Kutta (RK) scheme with multigrid and an implicit preconditioner has been shown to be an effective solver for the fluid dynamic equations. This scheme has been applied to both the compressible and essentially incompressible Reynolds-averaged Navier-Stokes (RANS) equations using the algebraic turbulence model of Baldwin and Lomax (BL). In this paper we focus on the convergence of the RK/implicit scheme when the effects of turbulence are represented by either the Spalart-Allmaras model or the Wilcox $k$-$\omega$ model, which are frequently used models in practical fluid dynamic applications. Convergence behavior of the scheme with these turbulence models and the BL model are directly compared. For this initial investigation we solve the flow equations and the partial differential equations of the turbulence models indirectly coupled. With this approach we examine the convergence behavior of each system. Both point and line symmetric Gauss-Seidel are considered for approximating the inverse of the implicit operator of the flow solver. To solve the turbulence equations we use a diagonally dominant alternating direction implicit (DDADI) scheme. Computational results are presented for three airfoil flow cases and comparisons are made with experimental data. We demonstrate that the two-dimensional RANS equations and transport-type equations for turbulence modeling can be efficiently solved with an indirectly coupled algorithm that uses the RK/implicit scheme for the flow equations.

**15. SUBJECT TERMS**

Aeronautics, Turbulence

| 16. SECURITY CLASSIFICATION OF: | | | 17. LIMITATION OF ABSTRACT | 18. NUMBER OF PAGES | 19a. NAME OF RESPONSIBLE PERSON |
|---|---|---|---|---|---|
| a. REPORT | b. ABSTRACT | c. THIS PAGE | | | STI Help Desk (email: help@sti.nasa.gov) |
| U | U | U | UU | 42 | **19b. TELEPHONE NUMBER** *(Include area code)* (301) 621-0390 |